



Durham E-Theses

The Study of Nanostructures in Organic Light-Emitting Diodes

JI, HONG

How to cite:

JI, HONG (2023) *The Study of Nanostructures in Organic Light-Emitting Diodes*, Durham theses, Durham University. Available at Durham E-Theses Online: <http://etheses.dur.ac.uk/15158/>

Use policy

The full-text may be used and/or reproduced, and given to third parties in any format or medium, without prior permission or charge, for personal research or study, educational, or not-for-profit purposes provided that:

- a full bibliographic reference is made to the original source
- a [link](#) is made to the metadata record in Durham E-Theses
- the full-text is not changed in any way

The full-text must not be sold in any format or medium without the formal permission of the copyright holders.

Please consult the [full Durham E-Theses policy](#) for further details.

The Study of Nanostructures in Organic Light-Emitting Diodes

Hong Ji

A thesis presented for the degree of
Masters by Research



Engineering Department
Durham University
United Kingdom
April 2023

不闻不若闻之，闻之不若见之，见之不若知之，知之不若行之。
学至于行之而止矣。

Abstract

This thesis presents research in the field of optoelectronic devices, specifically focusing on organic semiconductors (OSCs) employed as emitters within nanostructured arrays. The work encompasses both simulation and experimental aspects, each conducted separately. In the simulation section, two models grounded in the wave-particle duality of light were used to explore the impact of nanostructures on device performance. Following this, experimental investigations with nanostructured organic light-emitting diodes (OLEDs) substantiated the findings obtained from the simulations. A comparative analysis demonstrated that the presence of nanostructures led to an enhancement in key OLED properties when contrasted with non-structured OLEDs. Alongside these findings, the thesis provides a prospective roadmap for future research intended to maximize the performance of such devices.

Declaration

The work in this thesis is based on research carried out at the Engineering Department, Durham University, United Kingdom. No part of this thesis has been submitted elsewhere for any other degree or qualification and it is all my own work unless referenced to the contrary in the text.

Copyright © 2023 by Hong Ji.

“The copyright of this thesis rests with the author. No quotations from it should be published without the author’s prior written consent and information derived from it should be acknowledged”.

Acknowledgements

Thanks my research group, including my colleagues and supervisors.

感谢自己坚定地选择杜伦，感谢自己坚定地离开杜伦。
感谢帮助过我的每一个人。谢谢我的导师Mujeeb。谢谢Mana纯良的心，谢谢Kun对我生活上的照顾，谢谢Paloma成为我灯塔,尤其谢谢Adam给予我陪伴的力量。
谢谢我的家人和哥哥。
我会努力做自己的宇宙，长成一棵参天大树，给予我所爱之人们一片阴凉。

Contents

Abstract	iii
Declaration	iv
Acknowledgements	v
List of Abbreviations and Symbols	x
List of Figures	xii
List of Tables	xiv
1 Introduction	1
1.1 Motivation	1
1.2 Thesis Outline	2
Reference	4
2 Literature Review and Background	5
2.1 Organic Semiconductors and Applications	6
2.2 Organic Light-Emitting Devices	6
2.2.1 Working Principle of OLED	7
2.2.2 Energy Level of Organic Materials	8

2.3	Efficiencies of Emissive Devices	9
2.3.1	Internal Quantum Efficiency	9
2.3.2	External Quantum Efficiency	9
2.3.3	Optical (Outcoupling) Efficiency	10
2.4	Nanoimprint Lithography	12
2.4.1	Introduction on Lithography	12
2.4.2	Introduction on Nanoimprint Lithography	13
	Reference	24
3	Theoretical Background	25
3.1	COMSOL Multiphysics	26
3.1.1	Finite Element Method	26
3.1.2	Maxwell's Equation	28
3.2	OghmaNano	31
	Reference	33
4	Materials and Experimental Methods	34
4.1	Material Studied	35
4.2	Sample Preparation	35
4.2.1	Solution	35
4.2.2	Solid State Film	36
4.3	Fabrication Techniques	37
4.3.1	Spin Coating	37
4.3.2	Vacuum Thermal Evaporation	38
4.4	Electrical and Optical Characterizations	39
4.4.1	Set Up	39
4.4.2	Device Characterizations	40
4.5	Mechanical characterization	40
4.5.1	Atomic Force Microscopy	40
	Reference	43

5	Theoretical Results and Discussion	44
5.1	COMSOL Multiphysics	45
5.2	OghmaNano	48
	Reference	52
6	Experimental Results and Discussion	53
6.1	Nanostructure Fabrication	54
6.1.1	Introduction	54
6.1.2	Material Preparation	55
6.1.3	Experimental Procedure	56
6.1.4	Results	56
6.2	OLED Fabrication	58
6.2.1	Introduction	58
6.2.2	OLED pixel architecture	59
6.2.3	Material and Fabrication	59
6.2.4	Results	61
	Reference	66
7	Conclusion and Outlook	67
7.1	Conclusions	67
7.2	Future Work	68

List of Abbreviations and Symbols

AFM	Atomic force microscopy
Al	Alumina
Ag	Sliver
Cs ₂ CO ₃	Cesium carbonate
CVD	Chemical vapor deposition
DFB	Distributed feedback
EL	Electroluminescence
EML	Emissive layer
EQE	External quantum efficiency
ETL	Electron transport layer
FDTD	Finite-difference time-domain
FEM	Finite element method
HTL	Hole transport layer
HOMO	Highest occupied molecular orbital
IQE	Internal quantum efficiency
I-V	Current-voltage
LCD	Liquid-crystal display
LED	Light-emitting diode
LEFET	Light-emitting field-effect transistor
LUMO	Lowest unoccupied molecular orbital
MoO ₃	Molybdenum trioxide
Mw	molecular weight
NIL	Nano-imprint lithography
OLED	Organic light-emitting diode
OLET	Organic light-emitting transistor
OSC	Organic Semiconductor
PDMS	Polydimethylsiloxane
PhC	Photonic crystal
PVA	Poly(vinyl alcohol)
PML	Perfect match layer
PMMA	Poly(methyl methacrylate)
PMT	Photomultiplier tube
Si	Silicon
Si ₃ N ₄	Silicon Nitride
SMU	Source-measure unit
SPP	Surface plasmon polariton
Super Yellow	polyphenylene-vinylene (PPV)
TE	Transverse electric
TM	Transverse magnetic
TIR	Total internal reflection
UV	Ultraviolet
Al	Aluminium
Ag	Sliver
η_{out}	Outcoupling efficiency

List of Figures

2.1	The applications of organic semiconductors [23]	6
2.2	OLED Device architecture	7
2.3	Corresponding energy level diagram for Figure 2.2	8
2.4	Optical paths at the semiconductor/ambient interface	11
2.5	Kinds of light out-coupling losses in ordinary OLEDs [32]	12
2.6	Schematic diagram of technological processing for nanoimprint lithography technology [66]	14
3.1	Node placement and geometry for linear and second-order elements [4]	26
3.2	Electromagnetic Wave Propagation	30
4.1	Schematic diagram of spin-coating method [3]	37
4.2	Thermal evaporation process: resistive heating; electron beam source [8]	38
4.3	Thermal evaporation: basic design of evaporation sources [9]	39
4.4	The setup used for OLED testing	39
4.5	AFM working principle	40
5.1	Schematics of OLED architecture	45
5.2	The power increased by nanostructure compared with flat by percentage	47

5.3	Normalized Power ($\sqrt{E_x + E_y + E_z}$) intensity of horizontal and vertical dipole at wavelength of 680 and 430 nm for devices w/ or w/o nanograting	48
5.4	AFM images of fabricated devices with three nanostructures and the 3D-structures after reshape in software, The area used in the OGHMA Nano simulation was $10\mu m$ by $10\mu m$	49
5.5	The ray tracing simulation example	50
5.6	Spatial distribution of where the light hit the detector for three nanostructures	51
5.7	η_{out} vs Wavelength for a) Flat device, b) Grating Device	51
6.1	Thermal nanoimprinter lithography facility inside MEMS cleanroom	54
6.2	a) PVA master stamp, b) Diffraction grating sheet, c) Model Nano Pillars from PVA master stamp, d) Model Diffraction grating from grating sheet.	55
6.3	The AFM images of the nanopatterns	57
6.4	The height vs width of nanopattern	58
6.5	The structure of the fabricated OLED	58
6.6	The shadow mask design	59
6.7	The AFM images of nanograting on OLEDs	60
6.8	The height vs width	61
6.9	The reflection by eyes for flat and grating OLEDs	61
6.10	The light for flat and grating OLEDs with 10 V	62
6.11	(a) Current density and EL vs voltage for OLED (b) El vs voltage for OLED (log scale)	63
6.12	Spectrum of fabricated OLEDs	64
6.13	a) EQE vs Current density for Flat and Grating OLED architectures, b) EQE vs Luminance for Flat and Grating OLED architectures	65

List of Tables

4.1	Chemical structure of materials used in this thesis	35
5.1	OLED simulation parameters	45

CHAPTER 1

Introduction

1.1 Motivation

Organic light-emitting diodes (OLEDs) have emerged as promising contenders for lighting and display applications due to their numerous advantages over traditional light-emitting diodes (LEDs) and liquid-crystal displays (LCDs). However, they encounter a significant limitation: their external quantum efficiency (EQE) typically hovers around 20% [1]. This challenge primarily originates from the restricted light outcoupling efficiency (also known as light extraction efficiency), which is defined as the proportion of the light emitted outside the device to that generated within the device.

Enhancing the light outcoupling efficiency carries several advantages:

- **Brightness** Increasing the light outcoupling efficiency directly impacts the amount of light emitted from the OLED device. This enhancement means that more of the generated light successfully exits the device, effectively increasing its brightness. With more light escaping the OLED device, the resulting image or illumination appears more vibrant and clear to the human eye. This improvement is particularly beneficial for display applications where high brightness levels are needed, such as outdoor screens or high-dynamic-range television sets.

- **Energy Efficiency** OLEDs are already known for their high energy efficiency relative to conventional lighting and display technologies. However, by improving the light outcoupling efficiency, even less electrical energy would be required to generate a comparable amount of light. This efficiency translates to lower energy consumption for the same brightness level, reducing both operating costs and the device's environmental impact. This increased energy efficiency not only contributes to global carbon reduction efforts, but it also means that devices like OLED televisions or smartphone screens would consume less power, potentially extending battery life in portable devices.
- **Cost** By increasing the light outcoupling efficiency, each OLED device becomes more effective at producing light, thus requiring fewer or less intense light-emitting materials to achieve the same brightness level. This efficiency can decrease the need for costly high-intensity light sources or the quantity of organic compounds used, thereby reducing the overall manufacturing costs. Additionally, an increase in light outcoupling efficiency can also extend the OLED device's lifespan, decreasing the frequency of replacement, which also contributes to overall cost savings in the long run.

1.2 Thesis Outline

Chapter 2 establishes the research context, commencing with a succinct description of OSCs and organic emissive devices, followed by an exploration of OLEDs. It then delves into the challenges surrounding η_{out} and strategies to optimize it, primarily through integrating nanostructures. The chapter concludes with a comprehensive overview of nanostructure fabrication processes.

Chapter 3 elucidates the simulation theories utilized in this work, underpinned by two distinct software, COMSOL Multiphysics and OghmaNano. The initial section offers a theoretical methodology for wave propagation inside OLEDs, facilitated through COMSOL Multiphysics, alongside clarifications of the equations relevant to electromagnetic fields. This is succeeded by an outline of the simulation methodology grounded in OghmaNano, discussed in detail in Section 2.3.3.

Chapter 4 details the materials and experimental methods employed, including the chemical structures of the materials, sample preparations involving solutions and solid films, fabrication techniques like spin coating and vacuum thermal evaporation, and device characterizations, encompassing electrical, optical, and mechanical measurements.

Chapter 5 presents the simulations conducted using COMSOL and OghmaNano. The impact of various simulation environments and nanostructure sizes on η_{out} has been evaluated and contrasted with that of a flat OLED.

Chapter 6 highlights the experimental work involving nanostructure fabrication and the integration of these fabricated nanostructures into devices. It begins with a brief introduction to the user facility and material preparations, such as stamps and solutions, followed by the experimental procedure, and concludes with the AFM images of the fabricated nanopatterns.

Chapter 7 consolidates the insights garnered from Chapters 5 and 6, summarizing the main findings of this research.

Reference

- [1] N. C. Greenham, R. H. Friend, and D. D. Bradley, “Angular dependence of the emission from a conjugated polymer light-emitting diode: implications for efficiency calculations,” *Advanced Materials*, vol. 6, no. 6, pp. 491–494, 1994. 1.1, 2.1, 2.3.2

CHAPTER 2

Literature Review and Background

This chapter's objective is to lay the foundation of the research context. Initially, it provides a brief overview of OSCs and their application in optoelectronic devices, followed by an in-depth exploration of OLEDs. Furthermore, the focus shifts to η_{out} , a critical factor that substantially influences the performance of emissive devices, and the theoretical constraints that limit its optimization. Subsequently, the chapter offers an extensive exposition on potential strategies to enhance η_{out} , particularly through the integration of nanostructures. Ultimately, it concludes by detailing the fabrication processes associated with the nanostructures utilized in this project.

2.1 Organic Semiconductors and Applications

OSCs are built upon Π -conjugated carbon-based molecular or polymeric structures, which are bound together by comparatively weaker intermolecular interactions [1]. OSCs are gaining recognition as potential materials for the next wave of electronic applications, thanks to their distinguishing attributes such as lightweight nature, flexibility, and processability, which set them apart from their inorganic counterparts. OSCs have been applied into many fields [2, 3] including displays and lighting applications [4–6], electronic papers [7,8], thin-film batteries [9–11], supercapacitors [11–13], organic solar cells [14–16], sensors [17–19], and biosensors [20–22].

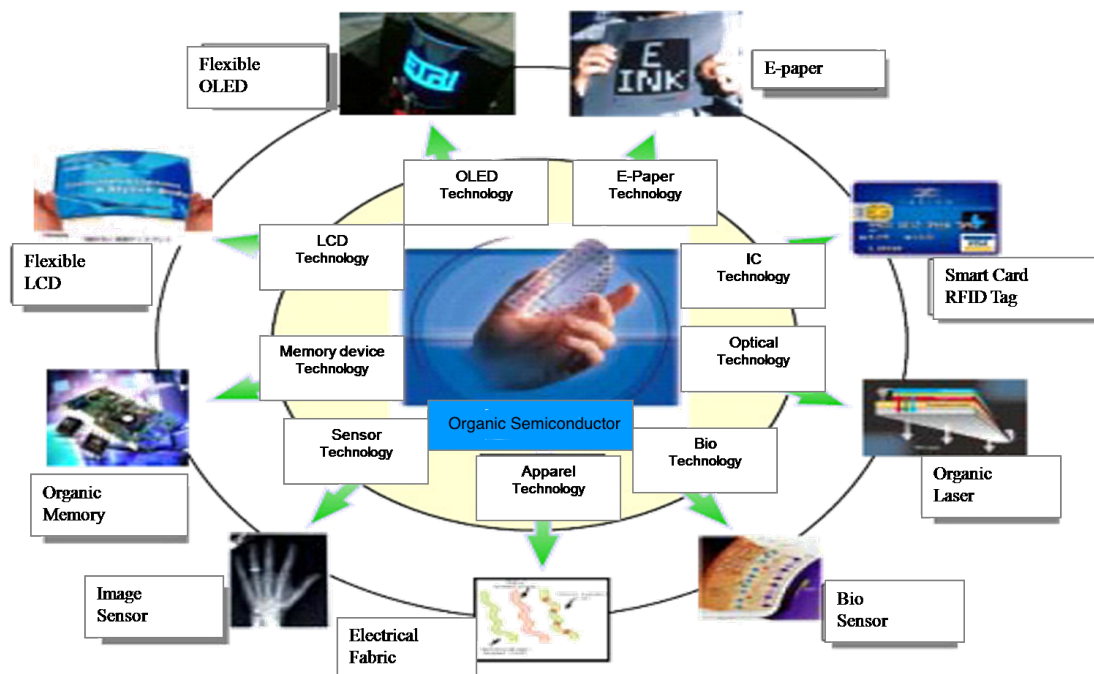


Figure 2.1: The applications of organic semiconductors [23]

2.2 Organic Light-Emitting Devices

In this project, the primary focus is on emissive devices that operate based on the principle of electroluminescence. This process involves the emission of light from the organic emissive material upon the application of an electric field. OLEDs and Light-emitting field-effect transistors (LEFETs) constitute significant portions of the organic light-emitting

device sector that employs semiconducting material. However, due to the constraints of time and the scope inherent in a Master by Research degree, the work presented here will exclusively address OLEDs. The architecture of OLEDs is depicted in Figure 2.2.

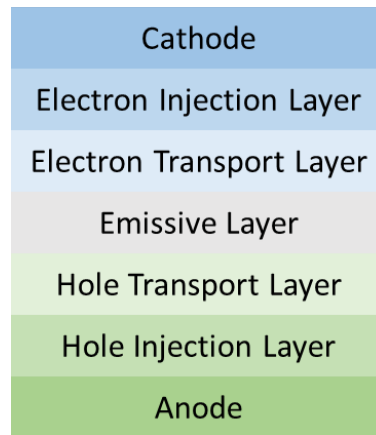


Figure 2.2: OLED Device architecture

2.2.1 Working Principle of OLED

An OLED comprises an organic thin film that serves as the emissive layer (EML), sandwiched between two inorganic/organic transport and injection layers, and electrodes (anode and a cathode). These electrodes facilitate the injection of opposite carriers, namely electrons and holes, into the organic emissive layer. When a voltage is applied, a stream of holes is generated in the hole injection layer (HIL), which moves towards the EML. The role of the hole transport layer (HTL) is to facilitate the movement of these holes by aiding their transport through the organic material.

Simultaneously, the applied voltage also drives a flow of electrons through the electron injection layer (EIL) and the electron transport layer (ETL). Upon reaching the EML, these electrons combine with the holes to form an exciton: a bound state of an electron-hole pair that is a fundamental electronic excitation in semiconductor crystals [24].

As these excitons transition to lower energy states, they emit light. The color of this light can be manipulated by changing the organic material used in the device.

2.2.2 Energy Level of Organic Materials

The electronic and optical characteristics of devices are significantly influenced by the Lowest Unoccupied Molecular Orbital (LUMO) and Highest Occupied Molecular Orbital (HOMO) energy levels of the organic materials utilized. These levels determine the energy barrier for the migration of electrons and holes, as well as the energy needed for light emission. When an OLED is powered on, electrons from the cathode are injected into the LUMO energy level of the organic material in the EML, while holes from the anode enter the HOMO level.

The energy difference between the HOMO and LUMO levels needs to align with the energy required for light emission. Simultaneously, altering energy levels can modulate the color of the light. If the LUMO level drops or the HOMO level rises, the energy required for light emission will decrease or increase, respectively. Consequently, the wavelength of the emitted light will become shorter or longer, changing the perceived color of the light. In Figure 2.3, the efficient injection and transport of charge carriers within the OLED

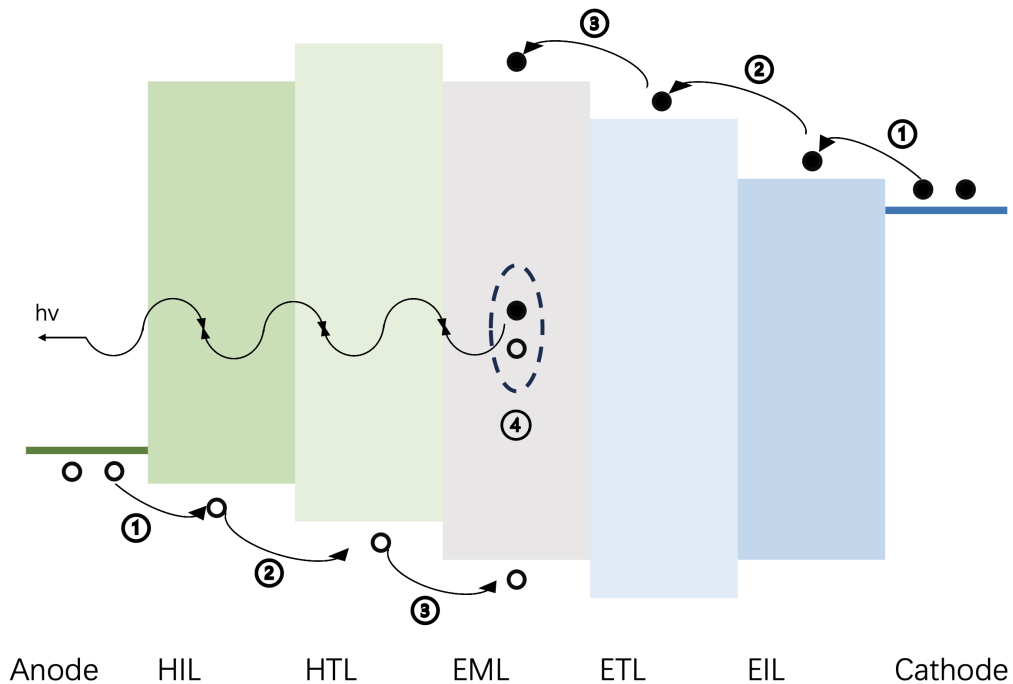


Figure 2.3: Corresponding energy level diagram for Figure 2.2

structure depend on the precise alignment of the energy levels and work functions of the various materials involved. By carefully selecting materials with appropriate work functions and energy levels, optimal charge injection and transport can be achieved, leading

to improved device performance and enhanced light emission. The proper alignment of energy levels and work functions enables smooth flow of electrons and holes from the anode and cathode, respectively, through the different layers of the device. This alignment minimizes energy barriers, allowing for efficient charge carrier movement and effective recombination within the emissive layer. Therefore, a thorough understanding and careful consideration of the energy level diagram and work functions are crucial in the design and optimization of OLED devices.

2.3 Efficiencies of Emissive Devices

Indeed, for applications in display and illumination, it's paramount that an OLED has a high capacity for converting electrical energy into light within the visible spectrum. This highlights the efficiency of the OLED as one of the key performance indicators.

2.3.1 Internal Quantum Efficiency

Internal Quantum Efficiency (IQE) η_{IQE} is the measurement of the efficiency of conversion of electrons and photons, defined as [25]:

$$\eta_{in} = \frac{\text{Number of the photons emitted from active region per second}}{\text{Number of the electrons injected inside the device per second}} = \frac{P_{in}/(hv)}{I/e}$$

where:

- P_{in} is the optical power emitted from the active region;
- I is the injection current.

2.3.2 External Quantum Efficiency

External Quantum Efficiency (EQE) is to give the ratio of the number of emitted light particles over the number of injected charge particles, defined as:

$$\eta_{ex} = \frac{\text{Number of the photons emitted into free space per second}}{\text{Number of the electrons injected inside the device per second}} = \frac{p/(hv)}{I/e}$$

where:

- p is the optical power emitted into free space.

EQE is commonly used as a representative performance indicator quantity when comparing differently emitting OLEDs [26], with the expression as the product of four main influencing parameters:

$$\eta_{ex} = \gamma * \eta_{rad,eff} * \eta_{S/T} * \eta_{out} = \eta_{in} * \eta_{out} \quad (2.1)$$

where:

- γ is the electrical efficiency. this factor is also referred to as charge balance, and it directly depends on the transport properties of the multilayer devices [27], which is nearly unity in optimized OLEDs [28];
- $\eta_{rad,eff}$ is the effective radiative efficiency, which accounts for the effectiveness of a certain emitter of the radiative and nonradiative rates [27];
- $\eta_{S/T}$ is the spin factor, which accounts for the share of excitons that are able to decay radiatively due to the quantum-mechanics spin selection rules [27];
- η_{out} is the outcoupling efficiency.

The expression of IQE can be also expressed as $\eta_{in} = \gamma * \eta_{rad,eff} * \eta_{S/T}$ based on the Equation 2.1. It can almost achieve 100% by using phosphorescent materials [4, 5]. However, the EQE of conventional OLEDs (bottom emission) was only 20% [6] without suitable photon management approaches.

2.3.3 Optical (Outcoupling) Efficiency

As a critical factor with significant room for improvement, the external quantum efficiency (EQE), η_{out} , is primarily influenced by the optical paths and interfaces within and around devices, rather than by electrical phenomena [24]. Its limitation stems from internal reflection at various interfaces due to refractive index mismatches between individual layers [29, 30]. This change in the path, controlled by the refractive indices of different materials, is also referred to as Snell's Law [31]:

$$\bar{n}_s \sin \theta_s = \bar{n}_o \sin \theta_o \quad (2.2)$$

where \bar{n}_s and \bar{n}_o are the refractive indexes of the semiconductor and ambient, respectively. Figure 2.4 depicts three scenarios occurring when light encounters the interface between

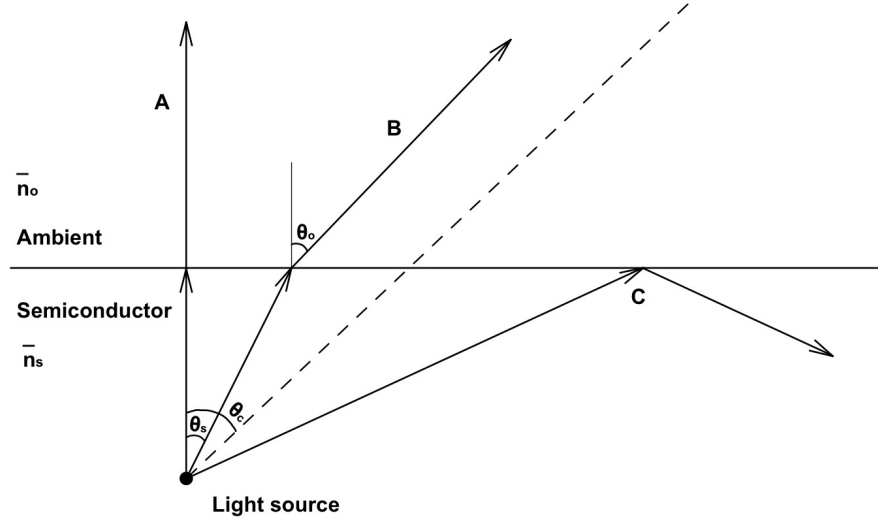


Figure 2.4: Optical paths at the semiconductor/ambient interface

the semiconductor and the ambient. In Scenario A, the incident light is normal to the surface, resulting in no change in its path direction. However, it may experience Fresnel loss at this interface, the reflection coefficient of which can be calculated as follows:

$$R = \left(\frac{\bar{n}_s - \bar{n}_o}{\bar{n}_s + \bar{n}_o} \right)^2 \quad (2.3)$$

When $\theta_s > 0^\circ$ and the refractive index of the semiconductor material \bar{n}_s is greater than \bar{n}_o (refractive index of air = 1), θ_o will always be larger than θ_s . When θ_s equals the critical angle θ_c , θ_o will become 90° and the refracted light will travel parallel to the interface. This critical angle defines the light-escape cone; any light hitting the interface at an angle larger than this value will be totally internally reflected back into the semiconductor. The critical angle can be calculated by substituting $\theta_o = 90^\circ$ into Equation 2.2:

$$\bar{n}_s \sin \theta_c = \bar{n}_o \sin 90^\circ$$

$$\theta_c = \sin^{-1} \left(\frac{\bar{n}_o}{\bar{n}_s} \right) \approx \frac{\bar{n}_o}{\bar{n}_s}$$

Organic layers typically have refractive indexes (n) ranging from 1.6 to 1.8, which are distinct from those of glass ($n_{glass} \approx 1.5$), air ($n_{air} = 1$), and the refractive indexes

of other layers within the device. These differences in refractive indexes create optical interfaces where total internal reflection (TIR) can occur, trapping a portion of the light in what are known as guided internal modes. As depicted in the following figure, outcoupling losses are attributed to several factors: surface plasmon polaritons (SPPs), waveguide modes, substrate modes, and electrode absorption. Extensive research on two-

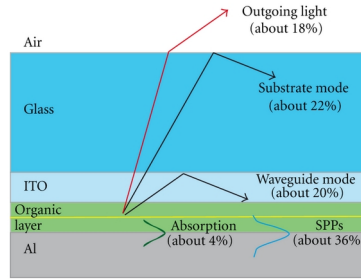


Figure 2.5: Kinds of light out-coupling losses in ordinary OLEDs [32]

dimensional periodic nanostructures has suggested that the external quantum efficiency, η_{out} , can be enhanced by altering the light path through the introduction of nanostructures within the device, such as photonic crystals (PhCs) and microlens arrays [32, 33]. Light can be efficiently extracted from the substrate mode by incorporating microlenses at the glass/air interface [34–36]. Moreover, PhCs and other nanostructures can be patterned onto the metal or organic layer to extract waveguide and surface plasmon polariton (SPP) modes [37–39]. Nevertheless, the fabrication process of nanostructures often faces challenges in controlling the shape of the nanostructures or in scaling up the area they cover. Another significant parameter in OLED optics is the orientation of the emitter dipole. It has been suggested that horizontally oriented dipoles could outperform vertically oriented ones, enhancing light extraction [40, 41]. However, studying this aspect forms the basis of a separate research project.

2.4 Nanoimprint Lithography

2.4.1 Introduction on Lithography

The fabrication of nanostructures has seen rapid advancements, primarily because of their potential to enhance the performance of optoelectronic devices. Apart from utilizing a

patterned mask to selectively remove certain areas deposited by chemical vapor deposition (CVD) [42], lithography is one of the most commonly employed processes to create the desired structures on a solid substrate (typically a Si-wafer). This is achieved by replicating a base or master pattern [43]. There are numerous subcategories within lithography [44], including:

- **Photolithography:** This method creates nanopatterns by transferring a targeted pattern on an optical mask to the surface [45–47].
- **Electron Beam (E-Beam) Lithography:** This technique employs focused electron beams to write on resists directly, enabling the creation of nanoscale patterns [48–50].
- **X-ray and Extreme UV Lithography:** These methodologies utilize intense near-ultraviolet light reflected from a mask onto a resist for nanofabrication [51–53].
- **Focused Ion Beam and Neutral Atomic Beam Lithography:** This form of lithography is a direct writing process using a narrow, scanning ion beam source, typically composed of gallium ions [54–56].
- **Soft Lithography:** Soft lithography employs elastomeric stamps, molds, and conformable photomasks to fabricate or replicate nanoscale structures. It is particularly known for utilizing polydimethylsiloxane (PDMS) as elastomeric materials [57–59].
- **Nanoimprint Lithography (NIL):** NIL is a simple mechanical lithography technique that forms the contours of a stamp by pressing the stamp onto a resist layer [60–62].

It is important to note that each lithography method has its unique advantages and application areas, and the choice of method will depend on the specific requirements of the project.

2.4.2 Introduction on Nanoimprint Lithography

Nanoimprint Lithography (NIL) has emerged as a promising candidate for next-generation lithography due to its low-cost, high volume, and wafer-scale patterning ability [63–65].

NIL is capable of achieving features in the nanometer scale and can pattern large areas, which is highly beneficial for industrial-scale production.

Three classic types of NIL, which include thermal NIL, UV-curable NIL, and micro/nano-contact NIL are illustrated in Figure 2.6. Thermal Nanoimprint Lithography (NIL), as

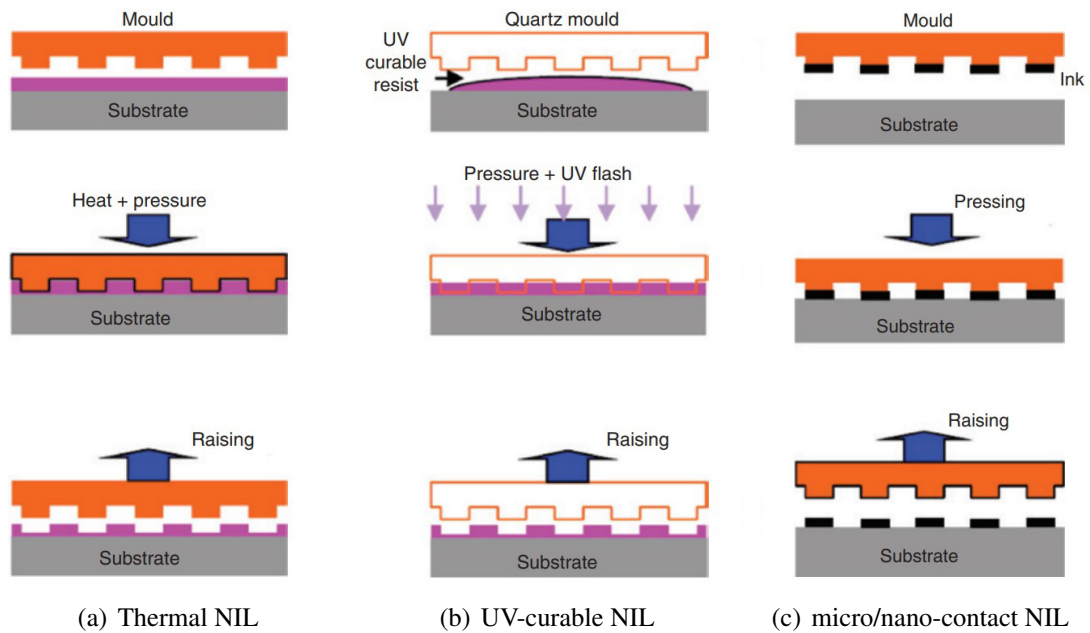


Figure 2.6: Schematic diagram of technological processing for nanoimprint lithography technology [66]

shown in Figure 2.6(a), is one of the earliest and most widely used techniques in the field. It was first invented by Stephen Chou in 1995, offering high resolution and cost-effectiveness [67]. In this technique, nanostructures are directly formed on a heated substrate surface, where the temperature exceeds the material's glass transition temperature, while applying a certain pressure.

UV Nanoimprint Lithography (UV-NIL), depicted in Figure 2.6(b), utilizes UV exposure polymerization at room temperature. Both techniques require additional processes, such as pattern transfer or etching, to remove residual materials.

Figure 2.6(c) illustrates contact NIL, where ink containing various materials, ranging from polymer solutions and living cells to DNA molecules and metallic films, is placed on a template and directly transferred to any surface with the desired patterns.

However, it should be noted that the high temperature and usage of harsh chemicals in some NIL techniques may damage or degrade organic materials, especially if the de-

sired pattern is on the organic layers. As a result, NIL is typically employed to fabricate nanopatterns on inorganic or supportive layers.

In this project, thermal pressing formation using a thermoplastic polymer as the resist material was the primary method for nanostructure fabrication [68]. By adjusting the pressure and temperature parameters, the height and curing time of the patterns can be controlled. The hot embossing process involves several steps, including:

- Cleaning the mold and substrate to prevent interference from contaminants or particles during the imprinting process.
- Raising the temperature of the polymer above its glass transition temperature.
- Placing the stamp on the substrate, ensuring even contact, and applying pressure to transfer the pattern from the mold to the substrate.
- Cooling the stamp and substrate to solidify the pattern and subsequently separating the stamp and substrate.

Reference

- [1] V. Gupta, “Chapter 1 - introduction and overview,” in *Molecular and Laser Spectroscopy*, V. Gupta and Y. Ozaki, Eds. Elsevier, 2020, pp. 1–40. [Online]. Available: <https://www.sciencedirect.com/science/article/pii/B9780128188705000010> 2.1
- [2] R. J. Martín-Palma and J. Martínez-Duart, *Nanotechnology for microelectronics and photonics*. Elsevier, 2017. 2.1
- [3] G. Nisato, D. Lupo, and S. Ganz, *Organic and Printed Electronics*. CRC Press, Taylor & Francis Group, 2016. 2.1
- [4] S. Reineke, F. Lindner, G. Schwartz, N. Seidler, K. Walzer, B. Lüssem, and K. Leo, “White organic light-emitting diodes with fluorescent tube efficiency,” *Nature*, vol. 459, no. 7244, pp. 234–238, 2009. 2.1, 2.3.2
- [5] G. Schwartz, S. Reineke, T. C. Rosenow, K. Walzer, and K. Leo, “Triplet harvesting in hybrid white organic light-emitting diodes,” *Advanced Functional Materials*, vol. 19, no. 9, pp. 1319–1333, 2009. 2.1, 2.3.2
- [6] N. C. Greenham, R. H. Friend, and D. D. Bradley, “Angular dependence of the emission from a conjugated polymer light-emitting diode: implications for efficiency calculations,” *Advanced Materials*, vol. 6, no. 6, pp. 491–494, 1994. 1.1, 2.1, 2.3.2
- [7] K. Amundson, J. Ewing, P. Kazlas, R. McCarthy, J. Albert, R. Zehner, P. Drzaic, J. Rogers, Z. Bao, and K. Baldwin, “12.3: Flexible, active-matrix display constructed using a microencapsulated electrophoretic material and an organic-semiconductor-based backplane,” in *SID Symposium Digest of Technical Papers*, vol. 32, no. 1. Wiley Online Library, 2001, pp. 160–163. 2.1
- [8] Y.-L. Loo, T. Someya, K. W. Baldwin, Z. Bao, P. Ho, A. Dodabalapur, H. E. Katz, and J. A. Rogers, “Soft, conformable electrical contacts for organic semiconductors: High-resolution plastic circuits by lamination,” *Proceedings of the National Academy of Sciences*, vol. 99, no. 16, pp. 10 252–10 256, 2002. 2.1
- [9] L. Bai, N. Wang, and Y. Li, “Controlled growth and self-assembly of multiscale organic semiconductor,” *Advanced Materials*, vol. 34, no. 22, p. 2102811, 2022. 2.1

- [10] A. F. Guedes, S. Tartari, V. P. Guedes, and I. J. Cunha, “Flexible organic battery technology applied in oled,” *Journal of Systemics Cybernetics and Informatics*, vol. 16, pp. 31–34, 2018. 2.1
- [11] C. Yumusak, A. J. Prochazkova, D. H. Apaydin, H. Seelajaroen, N. S. Sari-ciftci, M. Weiter, J. Krajcovic, Y. Qin, W. Zhang, J. Zhan *et al.*, “Indigoidine–biosynthesized organic semiconductor,” *Dyes and Pigments*, vol. 171, p. 107768, 2019. 2.1
- [12] S. Padmajan Sasikala, K. E. Lee, J. Lim, H. J. Lee, S. H. Koo, I. H. Kim, H. J. Jung, and S. O. Kim, “Interface-confined high crystalline growth of semiconducting polymers at graphene fibers for high-performance wearable supercapacitors,” *ACS nano*, vol. 11, no. 9, pp. 9424–9434, 2017. 2.1
- [13] S. K. Gupta, P. Jha, A. Singh, M. M. Chehimi, and D. K. Aswal, “Flexible organic semiconductor thin films,” *Journal of Materials Chemistry C*, vol. 3, no. 33, pp. 8468–8479, 2015. 2.1
- [14] A. F. Guedes, V. P. Guedes, S. Tartari, M. L. Souza, and I. J. Cunha, “New organic semiconductor materials applied in organic photovoltaic and optical devices,” *Journal of Systemics Cybernetics and Informatics*, vol. 13, pp. 38–40, 2015. 2.1
- [15] J. D. Myers and J. Xue, “Organic semiconductors and their applications in photovoltaic devices,” *Polymer Reviews*, vol. 52, no. 1, pp. 1–37, 2012. 2.1
- [16] S. Gélinas, A. Rao, A. Kumar, S. L. Smith, A. W. Chin, J. Clark, T. S. Van Der Poll, G. C. Bazan, and R. H. Friend, “Ultrafast long-range charge separation in organic semiconductor photovoltaic diodes,” *Science*, vol. 343, no. 6170, pp. 512–516, 2014. 2.1
- [17] D. A. Bernards, R. M. Owens, and G. G. Malliaras, “Organic semiconductors in sensor applications,” 2008. 2.1
- [18] Z. Wang, L. Huang, X. Zhu, X. Zhou, and L. Chi, “An ultrasensitive organic semiconductor no₂ sensor based on crystalline tips-pentacene films,” *Advanced Materials*, vol. 29, no. 38, p. 1703192, 2017. 2.1

- [19] P. Zhu, S. Li, X. Jiang, Q. Wang, F. Fan, M. Yan, Y. Zhang, P. Zhao, and J. Yu, “Non-invasive and wearable respiration sensor based on organic semiconductor film with strong electron affinity,” *Analytical chemistry*, vol. 91, no. 15, pp. 10 320–10 327, 2019. 2.1
- [20] J. Borges-González, C. J. Kousseff, and C. B. Nielsen, “Organic semiconductors for biological sensing,” *Journal of Materials Chemistry C*, vol. 7, no. 5, pp. 1111–1130, 2019. 2.1
- [21] C. Liao and F. Yan, “Organic semiconductors in organic thin-film transistor-based chemical and biological sensors,” *Polymer reviews*, vol. 53, no. 3, pp. 352–406, 2013. 2.1
- [22] J. Ta, W. Sun, and L. Lu, “Organic small molecule semiconductor materials for ofet-based biosensors,” *Biosensors and Bioelectronics*, p. 114667, 2022. 2.1
- [23] S. Saxena, “Organic semiconductor technology,” Exploring Electronics, blog, Feb. 26, 2012. [Online]. Available: <http://interactshradha.blogspot.com/2012/02/organic-semiconductor-technology.html> (document), 2.1
- [24] K. Seeger, *Semiconductor physics*. Springer Science & Business Media, 2013. 2.2.1, 2.3.3
- [25] E. Schubert and T. Gessmann, “Light emitting diodes,” in *Encyclopedia of Condensed Matter Physics*, F. Bassani, G. L. Liedl, and P. Wyder, Eds. Oxford: Elsevier, 2005, pp. 102–111. [Online]. Available: <https://www.sciencedirect.com/science/article/pii/B0123694019004988> 2.3.1
- [26] S. Reineke, M. Thomschke, B. Lüssem, and K. Leo, “White organic light-emitting diodes: Status and perspective,” *Reviews of Modern Physics*, vol. 85, no. 3, p. 1245, 2013. 2.3.2
- [27] O. Ostroverkhova, *Handbook of organic materials for electronic and photonic devices*, 2nd ed., 2018. 2.3.2

- [28] C. Adachi, M. A. Baldo, M. E. Thompson, and S. R. Forrest, “Nearly 100% internal phosphorescence efficiency in an organic light-emitting device,” *Journal of Applied Physics*, vol. 90, no. 10, pp. 5048–5051, 2001. 2.3.2
- [29] D. W. Kim, J. W. Han, K. T. Lim, and Y. H. Kim, “Highly enhanced light-outcoupling efficiency in ito-free organic light-emitting diodes using surface nanostructure embedded high-refractive index polymers,” *ACS applied materials & interfaces*, vol. 10, no. 1, pp. 985–991, 2018. 2.3.3
- [30] M. C. Gather and S. Reineke, “Recent advances in light outcoupling from white organic light-emitting diodes,” *Journal of Photonics for Energy*, vol. 5, no. 1, p. 057607, 2015. 2.3.3
- [31] F. Bryant, “Snell’s law of refraction,” *Physics Bulletin*, vol. 9, no. 12, p. 317, dec 1958. [Online]. Available: <https://dx.doi.org/10.1088/0031-9112/9/12/004> 2.3.3
- [32] Q. Yue, W. Li, F. Kong, and K. Li, “Enhancing the out-coupling efficiency of organic light-emitting diodes using two-dimensional periodic nanostructures,” *Advances in Materials Science and Engineering*, vol. 2012, 2012. (document), 2.5, 2.3.3, 5.1
- [33] K. Endo and C. Adachi, “Enhanced out-coupling efficiency of organic light-emitting diodes using an nanostructure imprinted by an alumina nanohole array,” *Applied Physics Letters*, vol. 104, no. 12, p. 121102, 2014. 2.3.3
- [34] C. Madigan, M.-H. Lu, and J. Sturm, “Improvement of output coupling efficiency of organic light-emitting diodes by backside substrate modification,” *Applied Physics Letters*, vol. 76, no. 13, pp. 1650–1652, 2000. 2.3.3
- [35] S. Möller and S. Forrest, “Improved light out-coupling in organic light emitting diodes employing ordered microlens arrays,” *Journal of Applied Physics*, vol. 91, no. 5, pp. 3324–3327, 2002. 2.3.3
- [36] W. H. Koo, H. J. Yun, F. Araoka, K. Ishikawa, S. M. Jeong, S. Nishimura, T. Toyooka, and H. Takezoe, “Spontaneously buckled microlens for improving outcoupled organic electroluminescence,” *Applied physics express*, vol. 3, no. 8, p. 082501, 2010. 2.3.3

- [37] Y. R. Do, Y. C. Kim, Y.-W. Song, C.-O. Cho, H. Jeon, Y.-J. Lee, S.-H. Kim, and Y.-H. Lee, “Enhanced light extraction from organic light-emitting diodes with 2d sio₂/sinx photonic crystals,” *Advanced Materials*, vol. 15, no. 14, pp. 1214–1218, 2003. 2.3.3
- [38] S. Jeon, J.-W. Kang, H.-D. Park, J.-J. Kim, J. R. Youn, J. Shim, J.-h. Jeong, D.-G. Choi, K.-D. Kim, A. O. Altun *et al.*, “Ultraviolet nanoimprinted polymer nanostructure for organic light emitting diode application,” *Applied Physics Letters*, vol. 92, no. 22, p. 200, 2008. 2.3.3
- [39] H.-H. Cho, B. Park, H.-J. Kim, S. Jeon, J.-h. Jeong, and J.-J. Kim, “Solution-processed photonic crystals to enhance the light outcoupling efficiency of organic light-emitting diodes,” *Applied optics*, vol. 49, no. 21, pp. 4024–4028, 2010. 2.3.3
- [40] D. Yokoyama and C. Adachi, “Horizontal molecular orientation in vacuum-deposited organic amorphous films,” in *WOLEDs and Organic Photovoltaics*. Springer, 2010, pp. 137–151. 2.3.3
- [41] J. Frischeisen, D. Yokoyama, C. Adachi, and W. Brütting, “Determination of molecular dipole orientation in doped fluorescent organic thin films by photoluminescence measurements,” *Applied Physics Letters*, vol. 96, no. 7, p. 29, 2010. 2.3.3
- [42] “Chapter 1 - deposition technologies: An overview,” in *Handbook of Deposition Technologies for Films and Coatings (Third Edition)*, third edition ed., P. M. Martin, Ed. Boston: William Andrew Publishing, 2010, pp. 1–31. [Online]. Available: <https://www.sciencedirect.com/science/article/pii/B9780815520313000016> 2.4.1
- [43] S. K. Sinha and A. Bit, “23 - microfluidics in tissue engineering,” in *Biomaterials for Organ and Tissue Regeneration*, ser. Woodhead Publishing Series in Biomaterials, N. E. Vrana, H. Knopf-Marques, and J. Barthes, Eds. Woodhead Publishing, 2020, pp. 567–598. [Online]. Available: <https://www.sciencedirect.com/science/article/pii/B9780081029060000106> 2.4.1
- [44] D. Sumanth Kumar, B. Jai Kumar, and H. Mahesh, “Chapter 3 - quantum nanostructures (qds): An overview,” in *Synthesis of Inorganic Nanomaterials*,

- ser. Micro and Nano Technologies, S. Mohan Bhagyaraj, O. S. Oluwafemi, N. Kalarikkal, and S. Thomas, Eds. Woodhead Publishing, 2018, pp. 59–88. [Online]. Available: <https://www.sciencedirect.com/science/article/pii/B9780081019757000038> 2.4.1
- [45] H. Tanaka, “13 - epitaxial growth of oxide films and nanostructures,” in *Handbook of Crystal Growth (Second Edition)*, second edition ed., ser. Handbook of Crystal Growth, T. F. Kuech, Ed. Boston: North-Holland, 2015, pp. 555–604. [Online]. Available: <https://www.sciencedirect.com/science/article/pii/B9780444633040000135> 2.4.1
- [46] M. Van Rossum, “Integrated circuits,” in *Encyclopedia of Condensed Matter Physics*, F. Bassani, G. L. Liedl, and P. Wyder, Eds. Oxford: Elsevier, 2005, pp. 394–403. [Online]. Available: <https://www.sciencedirect.com/science/article/pii/B0123694019005039> 2.4.1
- [47] T. Ishihara and X. Luo, “Chapter 17 - nanophotolithography based on surface plasmon interference,” in *Nanoplasmonics*, ser. Handai Nanophotonics, S. Kawata and H. Masuhara, Eds. Elsevier, 2006, vol. 2, pp. 305–312. [Online]. Available: <https://www.sciencedirect.com/science/article/pii/S1574064106800239> 2.4.1
- [48] J. Fu, L. Wu, G. Xi, and J. Tu, “New sensing technologies: Nanopore sensing,” in *Encyclopedia of Sensors and Biosensors (First Edition)*, first edition ed., R. Narayan, Ed. Oxford: Elsevier, 2023, pp. 581–597. [Online]. Available: <https://www.sciencedirect.com/science/article/pii/B9780128225486000601> 2.4.1
- [49] S. Prakash and J. Yeom, “Chapter 4 - advanced fabrication methods and techniques,” in *Nanofluidics and Microfluidics*, ser. Micro and Nano Technologies, S. Prakash and J. Yeom, Eds. William Andrew Publishing, 2014, pp. 87–170. [Online]. Available: <https://www.sciencedirect.com/science/article/pii/B9781437744699000044> 2.4.1
- [50] M. D. Charlton, “10 - photonic crystal nitride leds,” in *Nitride Semiconductor Light-Emitting Diodes (LEDs) (Second Edition)*, second edition ed., ser. Woodhead Publishing Series in Electronic and Optical Materials, J. Huang, H.-C. Kuo, and

- S.-C. Shen, Eds. Woodhead Publishing, 2018, pp. 327–376. [Online]. Available: <https://www.sciencedirect.com/science/article/pii/B9780081019429000101> 2.4.1
- [51] H. Radamson and L. Thyl'n, "Chapter 4 - moore's law for photonics and electronics," in *Monolithic Nanoscale Photonics: Electronics Integration in Silicon and Other Group IV Elements*, H. Radamson and L. Thyl'n, Eds. Oxford: Academic Press, 2015, pp. 121–150. [Online]. Available: <https://www.sciencedirect.com/science/article/pii/B9780124199750000040> 2.4.1
- [52] P. Nealey, M. Stoykovich, K. Yoshimoto, and H. Cao, "Nanolithographic polymer structures: Mechanical properties," in *Encyclopedia of Materials: Science and Technology*, K. J. Buschow, R. W. Cahn, M. C. Flemings, B. Ilschner, E. J. Kramer, S. Mahajan, and P. Veys'sire, Eds. Oxford: Elsevier, 2003, pp. 1–9. [Online]. Available: <https://www.sciencedirect.com/science/article/pii/B008043152601891X> 2.4.1
- [53] M. Kaestner, Y. Krivoshapkina, and I. W. Rangelow, "Chapter 14 - next generation lithography: the rise of unconventional methods?" in *Materials and Processes for Next Generation Lithography*, ser. Frontiers of Nanoscience, A. Robinson and R. Lawson, Eds. Elsevier, 2016, vol. 11, pp. 479–495. [Online]. Available: <https://www.sciencedirect.com/science/article/pii/B9780081003541000144> 2.4.1
- [54] R. Ambat and K. Piotrowska, "Chapter 8 - corrosion reliability testing, standards, and failure analysis," in *Humidity and Electronics*, R. Ambat and K. Piotrowska, Eds. Woodhead Publishing, 2022, pp. 339–380. [Online]. Available: <https://www.sciencedirect.com/science/article/pii/B9780323908535000086> 2.4.1
- [55] J. S. Lee, R. T. Hill, A. Chilkoti, and W. L. Murphy, "1.4.5 - surface patterning," in *Biomaterials Science (Fourth Edition)*, fourth edition ed., W. R. Wagner, S. E. Sakiyama-Elbert, G. Zhang, and M. J. Yaszemski, Eds. Academic Press, 2020, pp. 553–573. [Online]. Available: <https://www.sciencedirect.com/science/article/pii/B9780128161371000374> 2.4.1
- [56] T. Mahbub and M. E. Hoque, "Chapter 1 - introduction to nanomaterials and nanomanufacturing for nanosensors," in *Nanofabrication for Smart Nanosensor*

- Applications*, ser. Micro and Nano Technologies, K. Pal and F. Gomes, Eds. Elsevier, 2020, pp. 1–20. [Online]. Available: <https://www.sciencedirect.com/science/article/pii/B9780128207024000015> 2.4.1
- [57] M. Mateos-Timoneda, J. Planell, and E. Engel, “13 - modifying biomaterial surfaces for the repair and regeneration of nerve cells,” in *Surface Modification of Biomaterials*, ser. Woodhead Publishing Series in Biomaterials, R. Williams, Ed. Woodhead Publishing, 2011, pp. 325–343. [Online]. Available: <https://www.sciencedirect.com/science/article/pii/B9781845696405500130> 2.4.1
- [58] D. Riedel and B. Mizaikoff, “Chapter seven - surface imprinted micro- and nanoparticles,” in *Mip Synthesis, Characteristics and Analytical Application*, ser. Comprehensive Analytical Chemistry, M. Mar‘, Ed. Elsevier, 2019, vol. 86, pp. 153–191. [Online]. Available: <https://www.sciencedirect.com/science/article/pii/S0166526X19300741> 2.4.1
- [59] Z. Ahmad and A. M. Rahman, “Plastics in waveguide application,” in *Encyclopedia of Materials: Plastics and Polymers*, M. Hashmi, Ed. Oxford: Elsevier, 2022, pp. 295–315. [Online]. Available: <https://www.sciencedirect.com/science/article/pii/B9780128203521001632> 2.4.1
- [60] M. Kwiat, S. Cohen, A. Pevzner, and F. Patolsky, “Large-scale ordered 1d-nanomaterials arrays: Assembly or not?” *Nano Today*, vol. 8, no. 6, pp. 677–694, 2013. [Online]. Available: <https://www.sciencedirect.com/science/article/pii/S1748013213001175> 2.4.1
- [61] D. Resnick, “9 - nanoimprint lithography,” in *Nanolithography*, M. Feldman, Ed. Woodhead Publishing, 2014, pp. 315–347. [Online]. Available: <https://www.sciencedirect.com/science/article/pii/B9780857095008500099> 2.4.1
- [62] K. Mohamed, “2.16 - nanoimprint lithography for nanomanufacturing,” in *Comprehensive Nanoscience and Nanotechnology (Second Edition)*, second edition ed., D. L. Andrews, R. H. Lipson, and T. Nann, Eds. Oxford: Academic Press, 2019, pp. 357–386. [Online]. Available: <https://www.sciencedirect.com/science/article/pii/B9780128035818105089> 2.4.1

- [63] S. Y. Chou, P. R. Krauss, and P. J. Renstrom, "Imprint lithography with 25-nanometer resolution," *Science*, vol. 272, no. 5258, pp. 85–87, 1996. [Online]. Available: <https://www.science.org/doi/abs/10.1126/science.272.5258.85> 2.4.2
- [64] S. Y. Chou, P. R. Krauss, W. Zhang, L. Guo, and L. Zhuang, "Sub-10 nm imprint lithography and applications," *Journal of Vacuum Science & Technology B: Microelectronics and Nanometer Structures Processing, Measurement, and Phenomena*, vol. 15, no. 6, pp. 2897–2904, 1997. 2.4.2
- [65] C.-F. Wang, F.-C. Chang, and S.-W. Kuo, "Chapter 33 - surface properties of polybenzoxazines," in *Handbook of Benzoxazine Resins*, H. Ishida and T. Agag, Eds. Amsterdam: Elsevier, 2011, pp. 579–593. [Online]. Available: <https://www.sciencedirect.com/science/article/pii/B9780444537904000783> 2.4.2
- [66] Y.-G. Bi, J. Feng, J.-H. Ji, F.-S. Yi, Y.-F. Li, Y.-F. Liu, X.-L. Zhang, and H.-B. Sun, "Nanostructures induced light harvesting enhancement in organic photovoltaics," *Nanophotonics*, vol. 7, no. 2, pp. 371–391, 2018. (document), 2.6
- [67] S. Y. Chou, P. R. Krauss, and P. J. Renstrom, "Imprint of sub-25 nm vias and trenches in polymers," *Applied physics letters*, vol. 67, no. 21, pp. 3114–3116, 1995. 2.4.2
- [68] D. Andrews, T. Nann, and R. H. Lipson, *Comprehensive nanoscience and nanotechnology*. Academic press, 2019. 2.4.2

CHAPTER 3

Theoretical Background

The aim of this chapter is to provide the theoretical foundation for the simulations conducted in this project, utilizing two software tools: COMSOL Multiphysics and OghmaNano. The first part focuses on the theoretical methodology of simulation using COMSOL Multiphysics. This approach specifically addresses wave propagation within OLEDs and provides an explanation of the equations governing electromagnetic fields. The simulations in COMSOL Multiphysics enable the analysis of various aspects related to wave propagation, allowing for a deeper understanding of the optical behavior of OLEDs. The following section presents the methodology for simulation based on OghmaNano, which has been comprehensively detailed in Section 2.3.3. OghmaNano provides a specialized framework for simulating optical properties and outcoupling efficiency in nanostructured devices. The simulations conducted with OghmaNano offer insights into the impact of nanostructures on light extraction and provide valuable information for optimizing device performance. By employing these two software tools, a comprehensive analysis of the optical behavior and performance of OLEDs can be conducted, leading to a better understanding of the underlying physics and potential strategies for improving device efficiency and functionality.

3.1 COMSOL Multiphysics

3.1.1 Finite Element Method

In this project, the wave propagation inside OLEDs was analyzed using the finite element method (FEM) in a two-dimensional OLED geometry. The simulations were performed using COMSOL Multiphysics version 5.4, a widely used software tool for solving complex physical phenomena with geometrical and material non-linearities.

The FEM, first recognized for its utility by Richard Courant in 1943, has become a prominent numerical technique in various scientific and engineering fields. It is particularly effective for solving problems involving complex geometries and material properties. In this project, FEM was applied to perform mode analysis of optical waveguides within OLEDs, which possess arbitrary refractive index profiles and intricate waveguide structures [1, 2].

The FEM approach involves decomposing the complex problem region into interconnected finite elements or meshes, which cover the target surface and boundaries. These finite elements, also referred to as meshes, can adopt arbitrary shapes to ensure complete coverage of the problem domain [3]. Figure 3.1 illustrates the most common elements

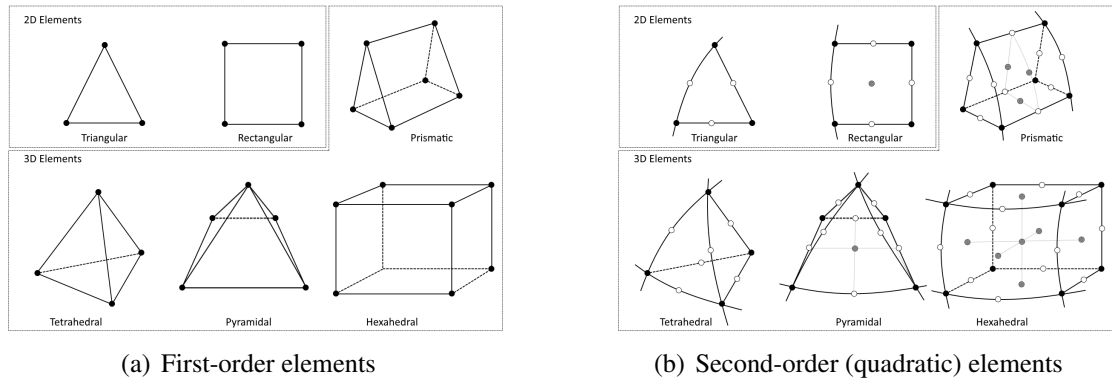


Figure 3.1: Node placement and geometry for linear and second-order elements [4]

used for meshing, where rectangular pieces in 2D (or hexahedral elements in 3D) are typically employed for structural mechanics analyses and boundary layer meshing.

By utilizing FEM in COMSOL Multiphysics, the wave propagation and optical behavior of OLEDs can be accurately simulated, providing valuable insights into the device's performance. The choice of FEM and the capability to generate appropriate meshes enable

a detailed analysis of optical waveguides and their complex behavior within the OLED structure. In addition to the discretization process, the interpolation function plays a crucial role in ensuring the accuracy of the FEM solution. The interpolation function is determined by the elements and their shared nodes within the finite element mesh. When the mesh is created, the positions X_i of the nodes are generated and stored. By using the known node positions X_i and the element shape function, any point between the nodes can be calculated. The choice of interpolation function is important as it affects the accuracy of the FEM solution. Finding the right balance between a large number of computationally efficient first-order elements and a smaller number of computationally expensive second-order elements is essential. This trade-off affects both the simulation time and the accuracy of the results. Using a large number of first-order elements may lead to faster computations but may sacrifice accuracy, while using a small number of second-order elements can provide higher accuracy but require more computational resources.

Within the FEM framework, the physical phenomena of interest can be modeled using governing equations and boundary conditions. These equations and conditions are approximately represented by the finite element algebraic equations. These equations describe the behavior of the system and are expressed in matrix form as:

$$[K]\{\mu\} = \{F\} \quad (3.1)$$

where:

- K describes the relationship between the forces applied to the system and the resulting displacements. It captures the mechanical properties and behavior of the system;
- F represents the external forces or loads applied to the system at each node of the finite element mesh. These forces can include applied loads, boundary conditions, or other external influences;
- μ represents the nodal vector which is the unknown vector that represents the deformation or response of the system at each node of the finite element mesh. It contains the values or degrees of freedom associated with the displacements or other variables of interest.

To solve the FEM equations, groups of linear equations are formulated using the stiffness matrix K and the nodal force vector F . These equations describe the behavior of the system within each finite element across the entire domain. The solution of these linear equations determines the values of the nodal vector μ , which provides information about the deformation or response of the system at each node.

The Galerkin method [5] is commonly used in FEM to obtain the solution of the linear equations. It involves multiplying the differential equations by a set of test functions and integrating over the entire domain. This process allows for the projection of the equations onto a finite-dimensional function space, resulting in a system of algebraic equations that can be solved to determine the nodal vector μ .

By solving these linear equations, the FEM provides an accurate representation of the system's behavior over each finite element within the entire domain. This enables the analysis and prediction of various physical phenomena and their effects on the system's response.

3.1.2 Maxwell's Equation

FEM is a robust and versatile numerical scheme to discretize electromagnetics problems and solve Maxwell's equations, which describe the behavior of electromagnetic fields in arbitrary geometric shapes. FEM is particularly effective when analyzing electromagnetic fields in steady-state or purely harmonic time-dependent scenarios in linear media [6].

Maxwell's equations in their differential or local form are a set of partial differential equations that govern the behavior of electric and magnetic fields. They can be expressed as follows:

- Gauss's Law:

$$\vec{\nabla} \cdot \vec{E} = \frac{\rho}{\epsilon_0}$$

- Gauss's Law for Magnetism:

$$\vec{\nabla} \cdot \vec{B} = 0$$

- Faraday's Law:

$$\vec{\nabla} \times \vec{E} = -\frac{d\vec{B}}{dt}$$

- Ampere & Maxwell's Law:

$$\vec{\nabla} \times \vec{B} = \mu_0 \left(\vec{J} + \epsilon_0 \frac{d\vec{E}}{dt} \right)$$

where:

- E is the electric field;
- B is the magnetic field;
- ρ is the charge density;
- J is the current density;
- ϵ_0 is the permittivity of free space;
- μ_0 is the permeability of free space;
- t is time.

To simulate Maxwell's equations using the finite element method (FEM), the simulation domain is discretized into a finite element mesh. Each finite element represents a small portion of the domain and is defined by a specific shape, such as triangles or quadrilaterals in 2D or tetrahedrons or hexahedrons in 3D.

Within each finite element, the electric and magnetic fields are approximated using a set of basis functions, also known as shape functions. These basis functions are typically polynomial functions defined over the element. The choice of the polynomial order depends on the desired accuracy of the solution, with higher-order polynomials providing more accurate approximations at the cost of increased computational complexity.

According to Equation 3.1, the unknown nodal values $\{\mu\}$, which are the coefficients of the basic functions, need to be determined. This process involves assembling the stiffness matrix $[K]$ and the nodal force vector F by accounting for the contributions from each finite element and incorporating appropriate boundary conditions. The resulting linear system can then be solved using numerical techniques, such as direct methods or iterative solvers.

Furthermore, the transverse electric (TE) and transverse magnetic (TM) modes in waveguides and resonant cavities also need to be considered when solving Maxwell's Equation

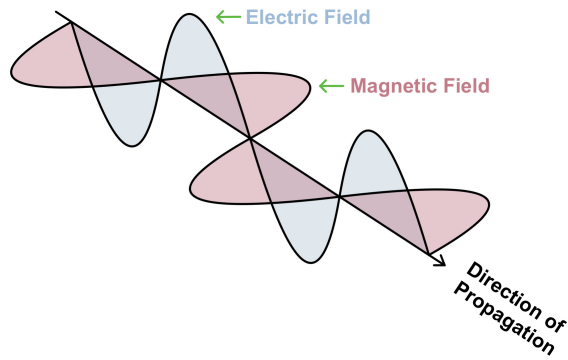


Figure 3.2: Electromagnetic Wave Propagation

with FEM. As shown in Figure 3.2, the electric field and the direction of the wave propagation are perpendicular without any part of an electric field in the direction of propagation inside TE mode. Similarly, in TM mode the magnetic field is totally transverse to the direction of wave propagation without any component of a magnetic field in the direction of propagation.

In TE mode, Maxwell's equations can be written in the form:

- $\nabla \times E = -j\omega\mu H$
- $\nabla \times H = j\omega\epsilon E$

In TM mode, Maxwell's equations can be written in the form:

- $\nabla \times E = -j\omega\mu H$
- $\nabla \times H = j\omega\epsilon E + j\omega\epsilon\delta n^2 E$

where:

- E is the electric field;
- H is the magnetic field;
- μ is the permeability of the medium;
- ϵ is the permittivity of the medium;
- j is the imaginary unit;
- ω is the angular frequency;

- δn is the refractive index of the medium.

Once the nodal values μ are obtained, the electric and magnetic fields can be reconstructed within each finite element by evaluating the linear combination of the basis functions using the nodal values. This provides a solution that approximates the behavior of the electromagnetic fields throughout the entire simulation domain.

By employing the FEM to solve Maxwell's equations, accurate and efficient simulations of electromagnetic phenomena can be achieved, facilitating the analysis and design of various devices and systems.

3.2 OghmaNano

The ray tracing simulation aims to replicate the behavior of light in a virtual environment, allowing us to visualize the path of light as it interacts with different layers or structures. This simulation calculates and displays the color and intensity of light that is reflected, transmitted, and absorbed by these layers.

In the simulation, the Fresnel Equation and Snell's Law, which have been explained in Section 2.3.3, are employed. These fundamental principles govern the behavior of light at interfaces and provide insights into the reflection, transmission, and absorption phenomena.

- **Reflection** As shown in Figure 2.4, the reflection will occur when the $\theta_s > \theta_c$. The light strikes the interface and bounces off at an angle equal to the angle of incidence. The amount of reflected light depends on factors such as the angle of incidence and the refractive index of the materials involved. The Fresnel equation (mentioned above in Equation 2.3) is used to calculate the amount of light reflected at each intersection point between a ray and a surface.
- **Transmission** Scenario B describes the transmission phenomenon, in which the light hits the interface and passes through it in the same direction. Similar to reflection, the amount of transmitted light is influenced by the angle of incidence of the light and the material properties, such as the refractive index. The Fresnel equation (mentioned above in Equation 2.3) is also employed to determine the quantity of

light transmitted at each intersection point between a ray and a surface.

- **Absorption** When the light does not continue to propagate, it means absorption. Absorption is slightly different from reflection and transmission because it influenced not only by the angle of incidence but also by the color and intensity of the incoming light. Usually, the percentage of absorption can be calculated by the formula:

$$\text{Absorption}\% = 1 - \text{Reflection}\% - \text{Transmission}\%$$

By understanding and quantifying the reflection, transmission, and absorption phenomena, we can gain valuable insights into the behavior of light in a virtual environment. These insights are essential for various applications, including the design and optimization of optical systems and the study of light-matter interactions.

Reference

- [1] F. Williamson, “Richard Courant and the finite element method: A further look,” *Historia Mathematica*, vol. 7, no. 4, pp. 369–378, 1980. [Online]. Available: <https://www.sciencedirect.com/science/article/pii/0315086080900014> 3.1.1
- [2] K. Okamoto, “Chapter 6 - finite element method,” in *Fundamentals of Optical Waveguides (Third Edition)*, third edition ed., K. Okamoto, Ed. Academic Press, 2022, pp. 271–338. [Online]. Available: <https://www.sciencedirect.com/science/article/pii/B9780128156018500069> 3.1.1
- [3] “Getting started with robust finite element method and solvers,” Cadence, blog, Oct 2022. [Online]. Available: <https://resources.system-analysis.cadence.com/blog/msa2020-getting-started-with-robust-finite-element-method-and-solvers> 3.1.1
- [4] “The finite element method (fem),” Multiphysics Cyclopedia, March 2016. [Online]. Available: [https://www.comsol.com/multiphysics/finite-element-method\(document\),3.1](https://www.comsol.com/multiphysics/finite-element-method(document),3.1)
- [5] V. Dolejší and M. Feistauer, “Discontinuous galerkin method,” *Analysis and Applications to Compressible Flow. Springer Series in Computational Mathematics*, vol. 48, p. 234, 2015. 3.1.1
- [6] “FDTD vs. fem vs. mom: What are they and how are they different?” Cadence, blog, Oct 2022. [Online]. Available: <https://resources.system-analysis.cadence.com/blog/msa2021-fdtd-vs-fem-vs-mom-what-are-they-and-how-are-they-different> 3.1.2

CHAPTER 4

Materials and Experimental Methods

Chapter 4 provides an overview of the data collection process, encompassing various aspects such as materials, sample preparation, data measurements, and device characterizations. The experimental techniques employed in this project can be broadly categorized into three groups: i. Fabrication techniques, which involves processes such as solution preparation, deposition of thin films, and any additional steps required to create the desired structures or configurations., ii. Electrical and optical characterizations, which involves conducting experiments to evaluate the performance of the fabricated OLEDs. Electrical measurements include assessing current-voltage characteristics, current density. Optical characterizations involve analyzing properties like emission spectra, luminance, EQE. iii. Mechanical characterization which assess the morphology of the thin-film surface.

4.1 Material Studied

Table 4.1 shows the polymer materials used for OLED fabrication and nanostructure fabrication.

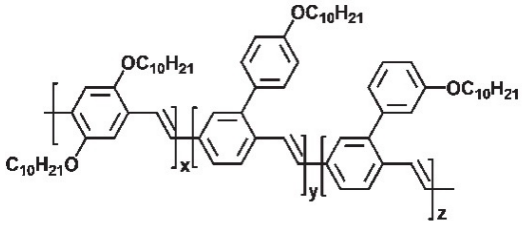
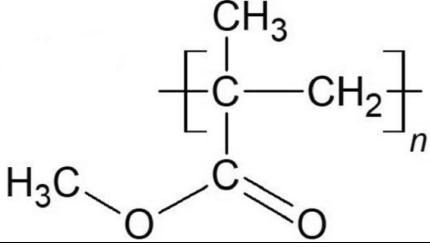
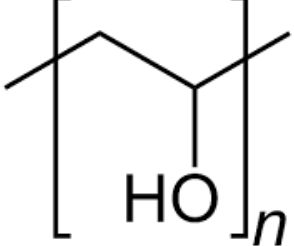
Chemical Structure	Name	Commercial Name
OLED Fabrication		
	poly(1,4-phenylenevinylene) (PPV)	Super Yellow
Nanostructure Fabrication		
	Polymethyl Methacrylate	PMMA
	Polyvinyl acetate	PVA

Table 4.1: Chemical structure of materials used in this thesis

4.2 Sample Preparation

4.2.1 Solution

During the solution preparation process, solutes and solvents are combined to create solutions. For instance, in the case of PMMA/Toluene, the solute is dissolved in the solvent using magnetic stirrers. The stirring process typically lasts for several hours, ranging from 2 to 24 hours, to ensure complete dissolution at room temperature. In certain instances, the solutions may be stirred at elevated temperatures (between 50 and 100 °C) to prevent

aggregation of low-solubility materials. The maximum temperature for achieving dissolution depends on the evaporation temperature of the solvent used.

It is important to note that the PVA solution utilized in this project requires degassing prior to use. When preparing the PVA/water solution with a concentration of 5 wt%, the solution must be subjected to degassing in a vacuum oven. This process removes any invisible bubbles present in the solution. Failure to remove these bubbles could have a detrimental effect on the light outcoupling efficiency during the fabrication of nanostructures.

By following these preparation steps, the solutions can be appropriately prepared for subsequent usage in the research project. It is crucial to ensure proper dissolution and degassing to obtain accurate and reliable results in the fabrication and characterization processes.

4.2.2 Solid State Film

Two types of solid-state films are employed in this project: i. Silicon substrates obtained from a commercial company, and ii. PVA films.

To fabricate PVA films, a mixture of PVA powder and water is prepared in a container with a weight percentage of 5 wt%. The solution is then heated at 90 °C using a magnetic stirrer for a duration of 2 hours. During this heating process, the solution gradually becomes transparent, indicating the dissolution of PVA. Subsequently, the solution is transferred to a vacuum oven to undergo a degassing process, which involves reducing the pressure to remove any dissolved gases.

Another degassing step occurs after pouring the PVA solution onto the stamp. This additional degassing process is performed to eliminate gas bubbles that may be present during the curing of the nanostructure. It is essential to ensure the complete removal of gas bubbles to achieve optimal fabrication results. The size of the PVA sheets should match that of the stamp used, or their dimensions can be verified using atomic force microscopy (AFM).

By following these procedures, PVA films can be prepared with controlled composition and minimized gas content, ensuring their suitability for subsequent processing steps and maintaining the integrity of the nanostructure fabrication process.

4.3 Fabrication Techniques

The fabrication of the devices studied in this work involved both solution processing and thermal evaporation techniques. A detailed explanation of these fabrication procedures is provided in Chapter 6. Here are brief descriptions of these techniques:

4.3.1 Spin Coating

Spin coating is a solution-based process developed for the low-cost deposition of a uniform polymer film in the micrometer to nanometer thickness range. Different parameters can control the thickness of the film. The expression for the film thickness can be found as [1, 2]:

$$h = \left(1 - \frac{\rho_A}{\rho_{A0}}\right) \cdot \left(\frac{3\eta \cdot m}{2\rho_{A0}\omega^2}\right)^{1/3} \quad (4.1)$$

where h is the thickness, ρ_A is density of volatile liquid (the mass of volatile solvent per unit volume), ρ_{A0} is the initial volume, η is viscosity of solution, m is rate of evaporation, and ω is angular velocity. Figure 4.1 shows the schematic diagram of the spin-coating method. An aspirator will fix the substrate on a plate. The prepared solution will be deposited onto the center of a wafer with a pipette. The centrifugal force achieved by the high-speed rotation will make a uniform distribution of materials across the whole surface of the substrate. After evaporating the coating solvent, the substrate can be used for the next fabrication process or repeat spin coating again with different materials. The advan-

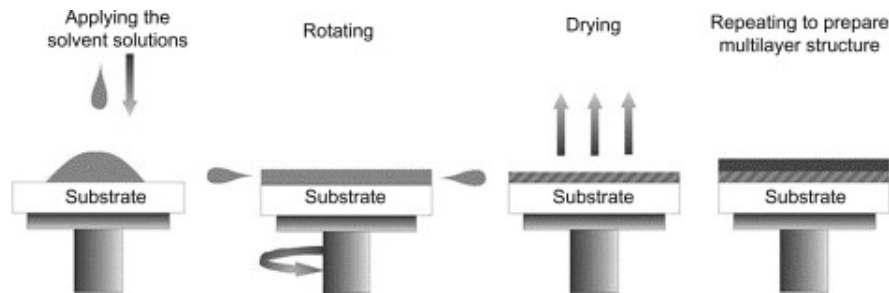


Figure 4.1: Schematic diagram of spin-coating method [3]

tages of spin coating are to achieve a good, thin, and uniform coating with a low-cost, quick, and easy procedure, while disadvantages are low material efficiency and incapable of the large scale of substrate [4, 5]. Normally only 2%-5% of solution can be dispensed

onto the substrate, while the rest solution is flung off and disposed of during the spin coating process, which is almost more than 95%. Besides, with the substrate scale increase, high-speed spinning will become difficult.

4.3.2 Vacuum Thermal Evaporation

Thermal evaporation is a physical vapor deposition technique that involves the vaporization of source materials from crucibles in a vacuum through high-temperature heating. The source material, in the form of vapor particles (atoms or molecules), condenses directly onto the substrate, transitioning back to a solid state [6]. The rate of evaporation is determined by the vapor pressure of the source material at the specified evaporation temperature. The term "thermal" emphasizes the importance of maintaining high temperatures during the process. Typically, normal crucibles can withstand Joule heating up to 2800 K, which generates significant vapor pressures for most metals.

The heating techniques employed in thermal evaporation can be categorized into two types: resistive heating and electron beam evaporation. When it comes to polymers, their poor thermal conductivity poses a challenge for resistive heating, while electron beam evaporation of organic materials is limited by the potential decomposition of the molecules [7]. Figure 4.2 illustrates these two thermal evaporation processes: In this

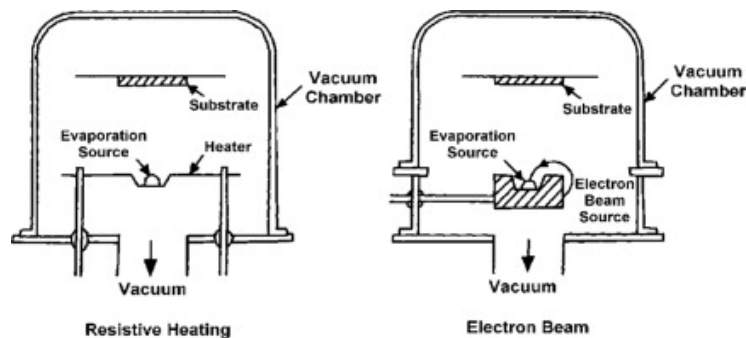


Figure 4.2: Thermal evaporation process: resistive heating; electron beam source [8]

particular study, only the resistive heating technique was utilized, employing two types of evaporation sources as depicted in Figure 4.3. The boat crucible was employed for powder materials, while the twisted wire was used for solid materials.

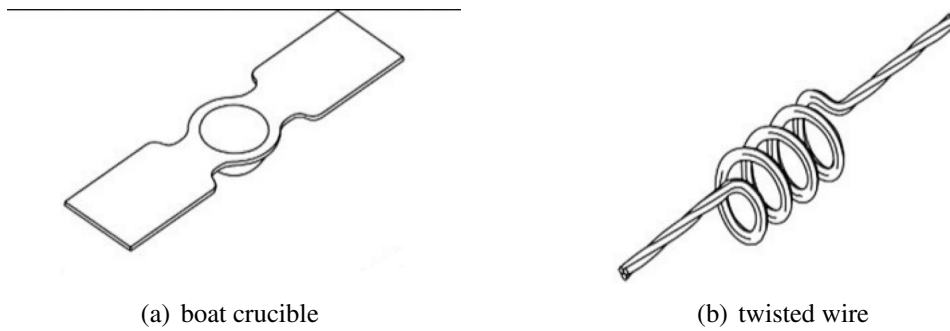


Figure 4.3: Thermal evaporation: basic design of evaporation sources [9]

4.4 Electrical and Optical Characterizations

4.4.1 Set Up

The experimental setup utilized in this study, as depicted in Figure 4.4, comprises several key components. These include a personal computer, a probe station, a source-measure unit (SMU), the OLED device being tested, and a photomultiplier tube (PMT). The DC

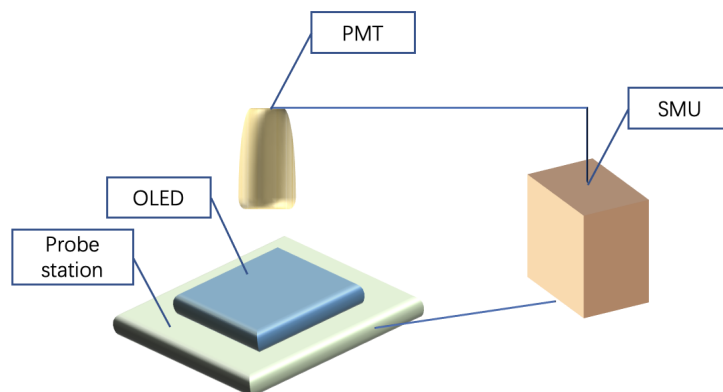


Figure 4.4: The setup used for OLED testing

voltage applied to the OLED is incrementally stepped from an initial value to an end value, with a specified interval. At each DC level, the system is given sufficient time to reach a steady-state condition, after which the measurements are averaged. This process ensures accurate and reliable data acquisition.

4.4.2 Device Characterizations

The current-voltage (IV) characteristics of the OLED were measured using an Agilent Technology B1500A semiconductor device analyzer. The device analyzer was connected to a probe station located inside a testing glove box, which was filled with nitrogen to provide a controlled environment. A voltage was applied between two electrodes, namely Alumina and Silver, to evaluate the performance of the fabricated OLED. Simultaneously, the photocurrent generated by the OLED was detected using a photomultiplier tube (PMT). Additionally, the electroluminescence (EL) spectral response of the OLED was measured using a USB4000 miniature fiber optic spectrometer. The spectrometer covered a wavelength range from 350 nm to 1050 nm.

4.5 Mechanical characterization

4.5.1 Atomic Force Microscopy

Atomic force microscopy (AFM) is one kind of observation method that takes advantage of the atomic force between the probe and the sample surface [10], which is usually used for micro/nanostructured coatings. The sharp tips inside AFM are around 10 to 20nm in diameter and are attached to a cantilever. The tips and cantilevers inside AFM are micro-fabricated with the material of Si or Si_3N_4 [11]. The movement of the tip based on the tip-surface interactions is measured by focusing a laser beam with a photodiode as depicted in Figure 4.5. There are two basic modes of AFM: contact and tapping modes.

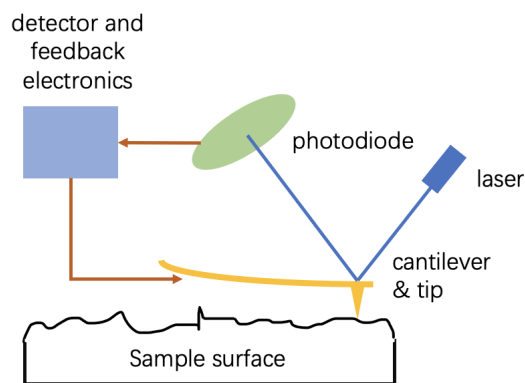


Figure 4.5: AFM working principle

The AFM tip continuously contacts the sample surface in the contact mode. While in tapping mode, the tip can be only in intermittent contact with the surface by the vibration of the cantilever. The AFM works for this project is the tapping mode, which can decrease the shear forces brought by the tip movement.

Reference

- [1] A. Mishra, N. Bhatt, and A. Bajpai, “Chapter 12 - nanostructured superhydrophobic coatings for solar panel applications,” in *Nanomaterials-Based Coatings*, ser. Micro and Nano Technologies, P. Nguyen Tri, S. Rtimi, and C. M. Ouellet Plamondon, Eds. Elsevier, 2019, pp. 397–424. [Online]. Available: <https://www.sciencedirect.com/science/article/pii/B9780128158845000120> 4.3.1
- [2] D. Bornside, C. Macosko, and L. Scriven, “Modeling of spin coating.” *Journal of imaging technology*, vol. 13, no. 4, pp. 122–130, 1987. 4.3.1
- [3] L. Dobrzański and M. Szindler, “Sol gel tio2 antireflection coatings for silicon solar cells,” *Journal of Achievements in Materials and Manufacturing Engineering*, vol. 52, no. 1, pp. 7–14, 2012. (document), 4.1
- [4] N. Sahu, B. Parija, and S. Panigrahi, “Fundamental understanding and modeling of spin coating process: A review,” *Indian Journal of Physics*, vol. 83, no. 4, pp. 493–502, 2009. 4.3.1
- [5] B. S. Yilbas, A. Al-Sharafi, and H. Ali, “Chapter 3 - surfaces for self-cleaning,” in *Self-Cleaning of Surfaces and Water Droplet Mobility*, B. S. Yilbas, A. Al-Sharafi, and H. Ali, Eds. Elsevier, 2019, pp. 45–98. [Online]. Available: <https://www.sciencedirect.com/science/article/pii/B9780128147764000033> 4.3.1
- [6] D. M. Mattox, “Deposition processes,” in *The Foundations of Vacuum Coating Technology*, D. M. Mattox, Ed. Norwich, NY: William Andrew Publishing, 2003, pp. 11–33. [Online]. Available: <https://www.sciencedirect.com/science/article/pii/B9780815514954500097> 4.3.2
- [7] J. Koskinen, “4.02 - cathodic-arc and thermal-evaporation deposition,” in *Comprehensive Materials Processing*, S. Hashmi, G. F. Batalha, C. J. Van Tyne, and B. Yilbas, Eds. Oxford: Elsevier, 2014, pp. 3–55. [Online]. Available: <https://www.sciencedirect.com/science/article/pii/B978008096532100409X> 4.3.2
- [8] K. Wasa, M. Kitabatake, and H. Adachi, “2 - thin film processes,” in *Thin Film Materials Technology*, K. Wasa, M. Kitabatake, and H. Adachi, Eds. Norwich,

NY: William Andrew Publishing, 2004, pp. 17–69. [Online]. Available: <https://www.sciencedirect.com/science/article/pii/B9780815514831500034> (document), 4.2

[9] F. L'vy, "Film growth and epitaxy: Methods," in *Reference Module in Materials Science and Materials Engineering*. Elsevier, 2016. [Online]. Available: <https://www.sciencedirect.com/science/article/pii/B9780128035818010122> (document), 4.3

[10] P. Liu and G. Chen, "Chapter nine - characterization methods: Basic factors," in *Porous Materials*, P. Liu and G. Chen, Eds. Boston: Butterworth-Heinemann, 2014, pp. 411–492. [Online]. Available: <https://www.sciencedirect.com/science/article/pii/B9780124077881000095> 4.5.1

[11] S. Sinha Ray, "4 - techniques for characterizing the structure and properties of polymer nanocomposites," in *Environmentally Friendly Polymer Nanocomposites*, ser. Woodhead Publishing Series in Composites Science and Engineering, S. Sinha Ray, Ed. Woodhead Publishing, 2013, pp. 74–88. [Online]. Available: <https://www.sciencedirect.com/science/article/pii/B9780857097774500048> 4.5.1

Theoretical Results and Discussion

This chapter shows the simulation results based on the theoretical study, which contains two separate software: COMSOL Multiphysics and OghmaNano. The simulations conducted in COMSOL Multiphysics provide insights into the electrical field distributions and power flow distributions within the simulated OLEDs. The chapter begins with a brief introduction to the simulation setup and the range of parameters used. The results are then visualized, allowing for a better understanding of the behavior and characteristics of the electrical fields. The quantified power results are also calculated and presented through plots and graphs, providing a comprehensive analysis of the simulation outcomes for power flows. In OghmaNano, the chapter starts by explaining the simulation settings employed in the software. The samples used in the simulations are described, along with the corresponding results obtained from the software. The chapter concludes with the presentation of the simulation results, which are plotted and analyzed to gain insights into the behavior and properties of the studied systems.

5.1 COMSOL Multiphysics

The software used in this study offers a platform for simulating the electric field using a two-dimensional finite element method. The calculation domain for the simulation is depicted in Figure 5.1, where the dimensions are specified using different symbols. In this simulation, the pitch length (λ) is set to 200 nm, and the spacing (s), height (h), and width (w) are all equal to 100 nm. The emission layer material employed in the simulation is Super Yellow, which has an emission wavelength ranging from 570 to 600 nm. Table 5.1 provides a summary of the parameters used in this simulation, providing a clear reference for the simulation setup and configuration. An electric point dipole is positioned

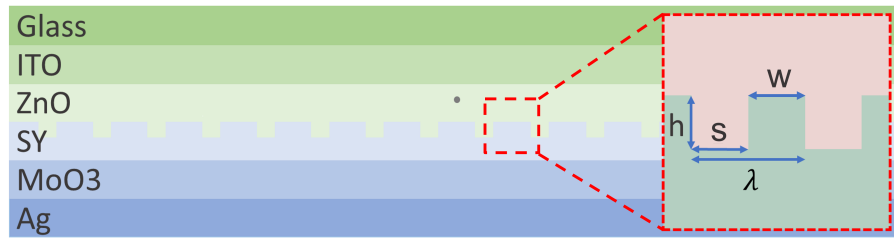


Figure 5.1: Schematics of OLED architecture

Table 5.1: OLED simulation parameters

Layer	Thickness (nm)	Range (nm)
Glass	1000	
Indium Tin Oxide (ITO)	80	
Zinc oxide (ZnO)	30	
Nanostructure	change	0, 20, 50, 100, 150, 200, 300
Super Yellow	change	from 150 to 500 with interval 25
Molybdenum trioxide (MoO3)	2	
Ag	100	

at the center of the device, serving as the input source for the simulation. The choice of an electrical point dipole as the excitation source is based on the understanding that electron-hole recombination can be effectively represented by a dipole [1]. While multiple dipole sources are commonly used in the simulation of three-dimensional methods, in practical applications, employing multiple dipole sources along with periodic continuation boundaries can lead to non-physical interference patterns that adversely affect device

performance [2]. In this study, a single dipole source within a finite computational domain was utilized to investigate the electrical intensity.

To mitigate reflections and simulate an open and non-reflecting infinite domain, a perfectly matched layer (PML) [3] is applied surrounding the entire simulation structure. The PML absorbs outgoing waves and suppresses reflections at the interface. To ensure effective absorption, the thickness of the PML should be at least half the size of the largest wavelength of interest.

Furthermore, an inhomogeneous mesh with varying grid sizes across different layers has been implemented in the simulation. This approach allows for accurate representation of the structures and phenomena within each layer, ensuring the fidelity of the simulation results.

To quantitatively compare the power flow between the flat and nanograting structures for output power, the net power flow out of the device will be calculated by the integration of the Poynting vector over the line topside the glass. For a given wavelength, the Poynting vector represents the instantaneous power flow per unit area and is given by:

$$\vec{S} = \vec{E} \times \vec{H} \quad (5.1)$$

where:

- E is the electric field
- H is the magnetic field

To calculate the net power flow out of the device, we integrate the Poynting vector over the line on the topside of the glass:

$$P_{out} = \int (\vec{E} \times \vec{H}) \cdot d\vec{L}_1 \quad (5.2)$$

where:

- L_1 is the line on which the Poynting vector integrated with

It is important to note that in this simulation, only the top side of the glass is considered for integration, as the output light is primarily expected to emerge from the top surface.

The magnitude of the electric current dipole moment is set to $1 \text{ A} \cdot \text{m}$, and therefore, only the output power is taken into account. Figure 5.2 illustrates the percentage increase

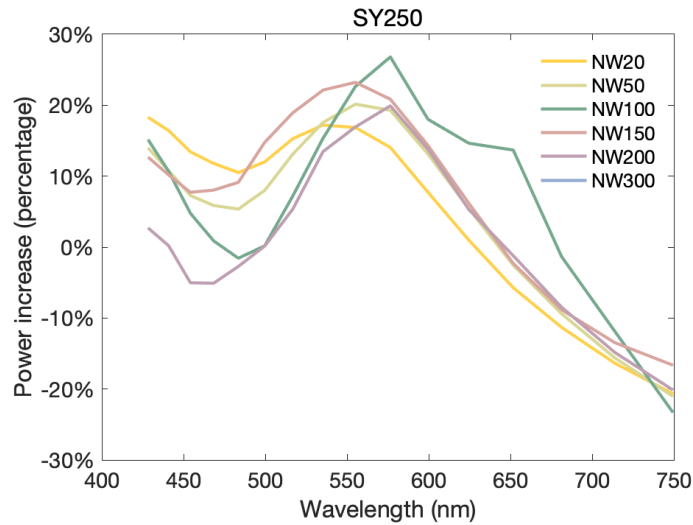


Figure 5.2: The power increased by nanostructure compared with flat by percentage

in power inside a nanograting structure compared to a flat OLED, as a function of the wavelength and size of the nanograting. The device structure optimization resulted in a significant 26.8% increase in power, particularly in the wavelength range around 580 nm. This improvement was achieved by utilizing a Super Yellow thickness of 250 nm and a nanostructure width of 100 nm.

Figure 5.3 showcases the distribution of the electrical field for horizontal and vertical dipoles at wavelengths of 430 nm and 680 nm, both with and without the nanograting structure. The results depicted in Figure 5.3 and Figure 5.2 clearly demonstrate that the nanograting structure leads to a substantial enhancement in the output power.

It is important to note that the simulations conducted in COMSOL represent an idealized scenario. In practical fabrication processes, it can be challenging to precisely replicate the same pattern as simulated. Various factors, such as material properties, deposition techniques, and process variations, can introduce deviations from the intended design. Therefore, there may be some discrepancies between the simulated results and the actual fabricated structures. Careful optimization and control during the fabrication process are necessary to achieve the desired pattern and maximize the performance of the device.

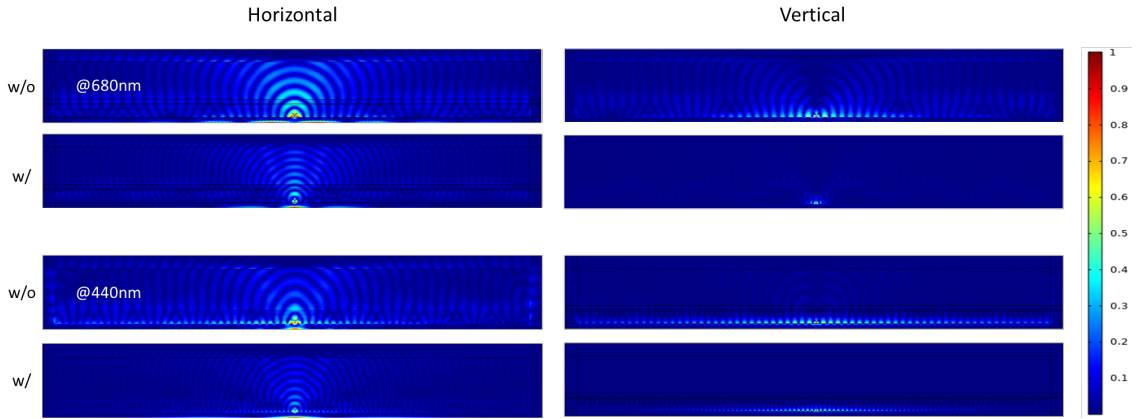


Figure 5.3: Normalized Power ($\sqrt{E_x + E_y + E_z}$) intensity of horizontal and vertical dipole at wavelength of 680 and 430 nm for devices w/ or w/o nanograting

5.2 OghmaNano

The ray tracing simulation performed in OghmaNano utilizes the AFM image of the patterned surface as a basis for the simulation [4–6]. The image is used to generate a mesh that represents the nanostructure on the designated layer. The simulation then calculates the outcoupling efficiency, which represents the percentage of emitted light that escapes the device and reaches the detector.

In the simulation, light sources within the emission layer serve as the input source, simulating the light generated within the layer. A detector is placed slightly above the emission layer to collect the light that escapes from the device. The detector measures the amount of light that reaches it, taking into account the absorption within materials and the reflection trapped inside the device.

The outcoupling efficiency is calculated as the ratio of the detected light to the emitted light, indicating how efficiently the emitted light is captured by the detector. Additionally, the simulation can provide a spatial distribution map, showing where the light hits the detector.

The simulation data obtained from the flat device serves as the reference for comparison, allowing the assessment of improvements in escape efficiency. The simulated wavelength range spans from 450 to 700 nm, with 100 sample points within that range.

Figure 5.4 illustrates the AFM images of three different types of nanostructures that were used in the simulation for efficiency calculation. Each AFM image represents the surface

morphology of the corresponding nanostructure. In the simulation, these AFM images are utilized to reshape the nanostructures in OghmaNano, resulting in their respective 3D structures.

The reshaping process in OghmaNano ensures that the simulated nanostructures accurately represent the real surface morphology captured by the AFM images. This allows for a more precise simulation of the optical properties and outcoupling efficiency of the nanostructures. Figure 5.5 depicts an example of a ray tracing simulation conducted in

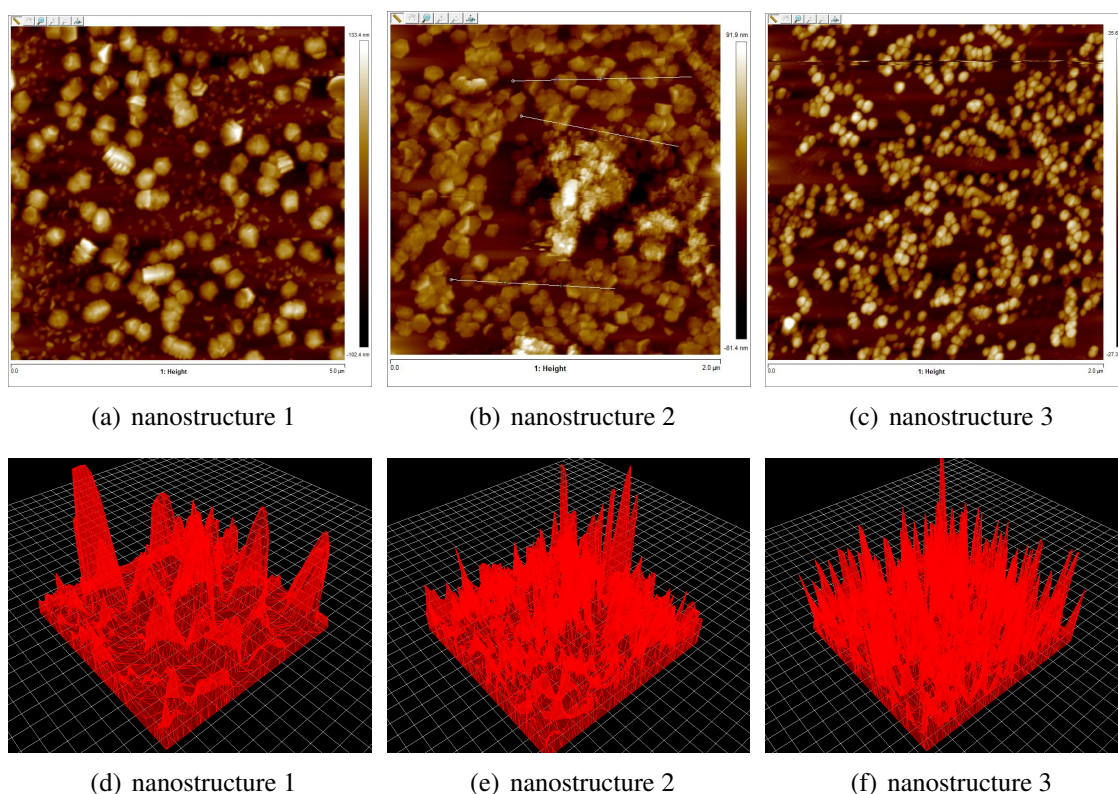


Figure 5.4: AFM images of fabricated devices with three nanostructures and the 3D-structures after reshape in software, The area used in the OGHMA Nano simulation was $10\mu m$ by $10\mu m$

OghmaNano. The simulation involves a nanostructure made of ZnO material and an emission layer composed of Super Yellow. In this simulation, different colors are used to represent the tracing of light at different wavelengths. This visualization provides insight into how light behaves and propagates within the simulated nanostructure, allowing for the analysis of light-matter interactions and the evaluation of the device's performance. Figure 5.6 presents the spatial distribution results obtained from the visualization of light reaching the detector in the ray tracing simulations. The analysis reveals that for the three

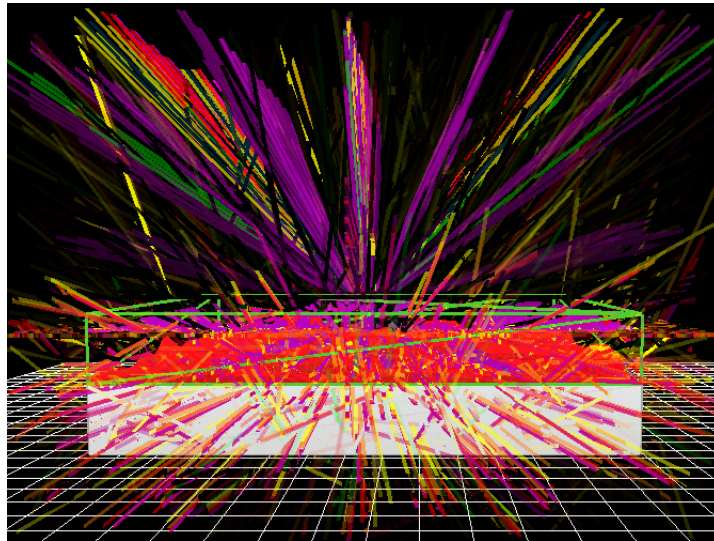


Figure 5.5: The ray tracing simulation example

different nanostructures, more light is observed to escape outside the film compared to the flat structure. This increase in light outcoupling is particularly prominent at a wavelength of around 580nm. These findings suggest that the introduction of nanostructures can significantly enhance the efficiency of light extraction in the simulated devices. Figure 5.7 presents the simulation results and optimization of different nanostructures in terms of outcoupling efficiency. It can be observed that the performance of the nanostructure devices is superior to that of the flat device, with a significant increase in η_{out} in the wavelength range of 500 to 590nm. Among the nanostructure devices, nanostructure 1 and 2 demonstrate a more pronounced improvement in η_{out} at yellow light wavelengths compared to nanostructure 3. Furthermore, the nanostructure 1 device exhibits slightly better performance than the other nanostructures. These findings indicate that the specific design and characteristics of the nanostructures play a crucial role in enhancing the outcoupling efficiency of the devices.

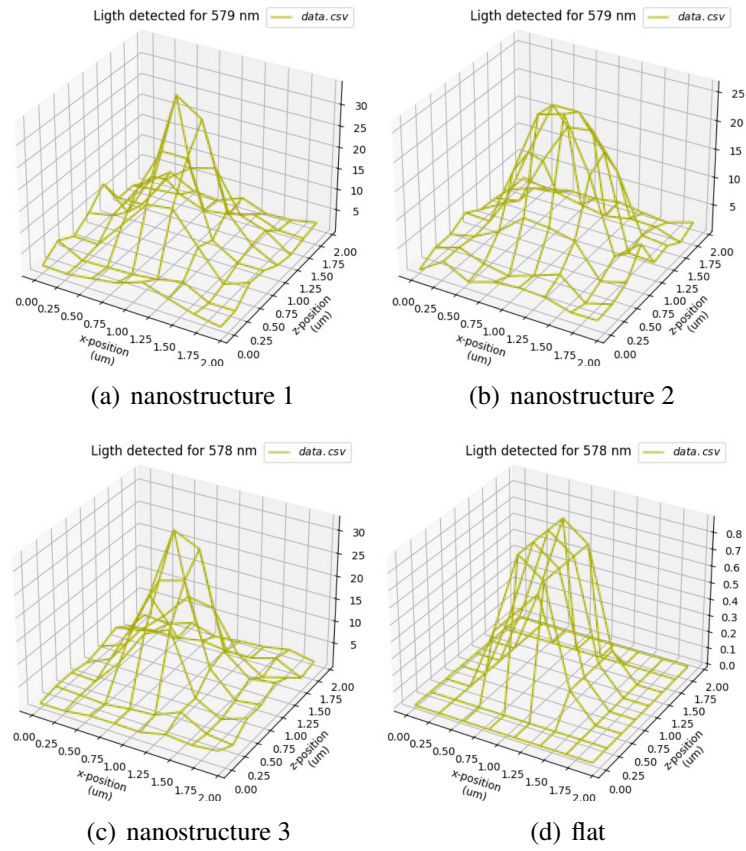


Figure 5.6: Spatial distribution of where the light hit the detector for three nanostructures

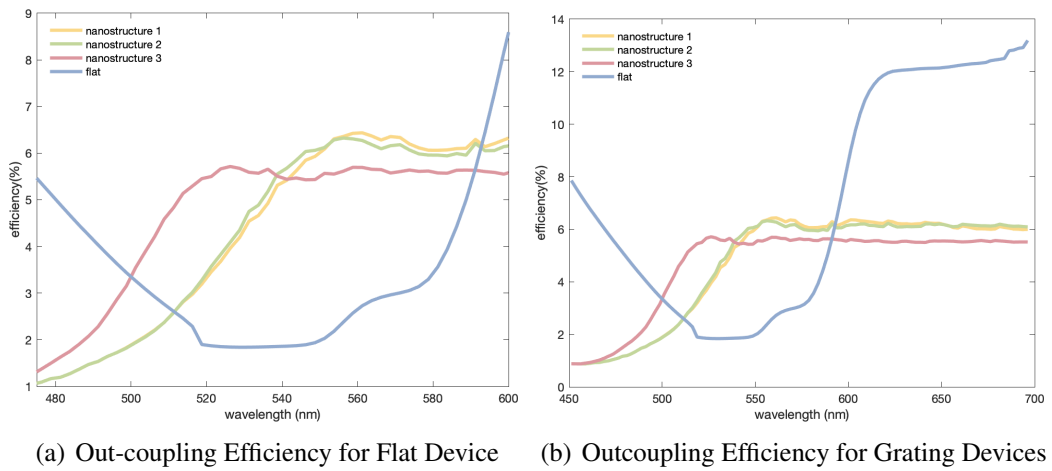


Figure 5.7: η_{out} vs Wavelength for a) Flat device, b) Grating Device

Reference

- [1] H. Benisty, R. Stanley, and M. Mayer, “Method of source terms for dipole emission modification in modes of arbitrary planar structures,” *Journal of The Optical Society of America A-optics Image Science and Vision*, vol. 15, pp. 1192–1201, 1998. 5.1
- [2] Q. Yue, W. Li, F. Kong, and K. Li, “Enhancing the out-coupling efficiency of organic light-emitting diodes using two-dimensional periodic nanostructures,” *Advances in Materials Science and Engineering*, vol. 2012, 2012. (document), 2.5, 2.3.3, 5.1
- [3] J.-P. Berenger, “A perfectly matched layer for the absorption of electromagnetic waves,” *Journal of computational physics*, vol. 114, no. 2, pp. 185–200, 1994. 5.1
- [4] R. Singh, E. Aluicio-Sarduy, Z. Kan, T. Ye, R. MacKenzie, and P. E. Keivanidis, “Fullerene-free organic solar cells with an efficiency of 3.7% based on a low-cost geometrically planar perylene diimide monomer,” *Journal of Materials Chemistry A*, vol. 2, no. 35, pp. 14 348–14 353, 2014. 5.2
- [5] L. Sims, U. Hörmann, R. Hanfland, R. C. MacKenzie, F. R. Kogler, R. Steim, W. Brütting, and P. Schilinsky, “Investigation of the s-shape caused by the hole selective layer in bulk heterojunction solar cells,” *Organic Electronics*, vol. 15, no. 11, pp. 2862–2867, 2014. 5.2
- [6] Y. Gao, R. C. MacKenzie, Y. Liu, B. Xu, P. H. Van Loosdrecht, and W. Tian, “Engineering ultra long charge carrier lifetimes in organic electronic devices at room temperature,” *Advanced Materials Interfaces*, vol. 2, no. 4, p. 1400555, 2015. 5.2

CHAPTER 6

Experimental Results and Discussion

This chapter presents the experimental results obtained from the fabrication and integration of the nanostructures into OLED devices. The first section provides a detailed description of the fabrication process for the nanostructures, outlining the specific steps involved. Following this, the integration of the fabricated nanostructures into the OLED devices is discussed, highlighting the improvements achieved in the device performance. The experimental results demonstrate that the integration of the nanostructures has successfully enhanced the performance of the OLED devices. The specific improvements observed in terms of device efficiency, light extraction, or other relevant parameters are detailed and analyzed. These results validate the effectiveness of the nanostructure fabrication and integration process in enhancing the overall performance of the OLED devices.

6.1 Nanostructure Fabrication

6.1.1 Introduction

The thermal nanoimprint lithography (NIL) process was conducted within the MEMS cleanroom facility, utilizing the equipment shown in Figure 6.1. The equipment consists of an upper part for applying pressure and a lower hot plate for supplying heat. To con-

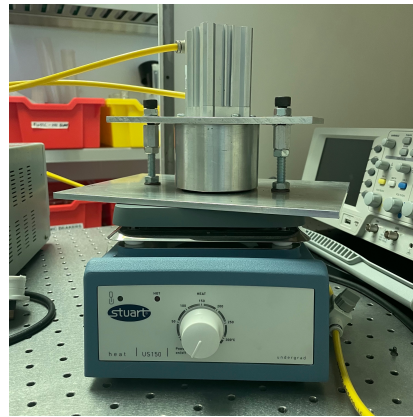


Figure 6.1: Thermal nanoimprinter lithography facility inside MEMS cleanroom

control the pressure applied to the substrate, the screws on both sides of the imprinter can be adjusted. By turning these screws, the pressure can be increased or decreased as required for the specific imprinting process.

The temperature during the thermal NIL process is controlled by the rotator on the hot plate. The rotator allows for precise temperature adjustments to achieve the desired softening and flow of the resist material.

After the imprinting process, the quality and accuracy of the pattern achieved can be verified visually by examining the reflection of light or by using atomic force microscopy (AFM) imaging. These verification methods provide insights into the replication fidelity and the overall quality of the fabricated nanostructures.

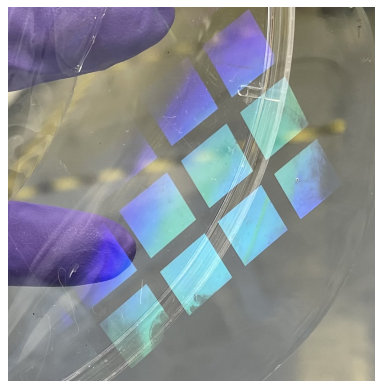
In the upcoming Section 6.1.4, the results of the thermal NIL process will be presented, including the verification of the pattern using AFM images and discussions on the challenges encountered and potential improvements that can be made based on the findings.

6.1.2 Material Preparation

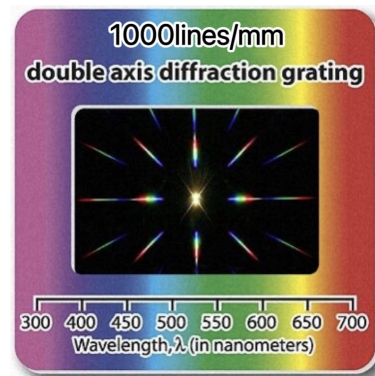
Stamps

Two types of stamps were used in this work to create patterns on the PMMA surface. The first type of stamp was made from Poly(vinyl alcohol) (PVA) sheets, which were the same product used in Section 6.2. The geometric model of the PVA sheet stamp is shown in Figure 6.2(c), which depicts the surface shape of the PVA sheet with specific dimensions including pitch, width, and height (400 nm, 200 nm, and 150 nm, respectively). The second type of stamp used was a diffraction grating sheet, which was commercially purchased. The surface shape of the diffraction grating sheet stamp, with a linear size of 1000 lines/mm, is illustrated in Figure 6.2(d).

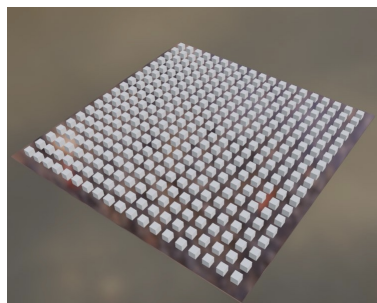
Both types of stamps were designed with specific geometric patterns to create the desired nanostructures on the PMMA surface during the thermal nanoimprint lithography process.



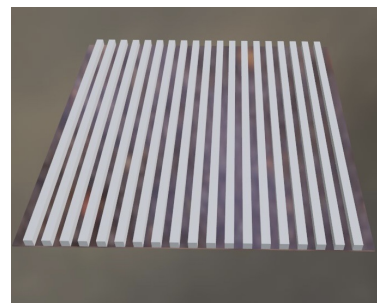
(a) PVA sheets



(b) grating sheets



(c) PVA sheets



(d) grating sheets

Figure 6.2: a) PVA master stamp, b) Diffraction grating sheet, c) Model Nano Pillars from PVA master stamp, d) Model Diffraction grating from grating sheet.

PMMA solution (70mg/ml in Toluene)

To prepare the PMMA/Toluene solution, 350 mg of PMMA with a molecular weight of 120,000 was dissolved in 5 ml of Toluene. The mixture was stirred using magnetic stirrers for 24 hours at a temperature of 80°C. During the stirring process, the PMMA gradually dissolved in the Toluene solvent. After 24 hours, the solution reached a point where it became transparent, indicating that the PMMA had completely dissolved without any impurities. The resulting solution had a concentration of 70 mg/ml of PMMA in Toluene.

6.1.3 Experimental Procedure

To fabricate the imprint, the PMMA solution was spin-coated onto the glass substrate. The spin-coating process involved two steps. First, the solution was spun at a speed of 500 rpm for 10 seconds to ensure a uniform coating. Then, the speed was increased to 1750 rpm for 30 seconds to achieve the desired thickness of the PMMA layer. After the spin-coating process, the PMMA-coated substrate was pre-baked at 100°C for 3 minutes to remove any residual solvent.

Next, the stamp sheet with the nanostructure was placed on top of the PMMA layer. The imprinter was heated to a temperature of 200°C (or 180°C for PVA sheets as the PVA will degrade above 200°C [1]) and pressed onto the PMMA surface. The pressure applied during the imprinting process was controlled by turning the screws on both sides of the imprinter, although precise quantization of pressure was not possible.

The imprinter was kept in contact with the PMMA surface at the elevated temperature for 30 minutes to allow for the transfer of the nanostructure pattern. After the 30-minute baking process, the imprinter was allowed to cool down for 20 minutes. This cooling period allowed the PMMA to solidify and cure, effectively preserving the shape of the pattern.

The resulting structure consisted of the patterned PMMA layer on top of the glass substrate, with the nanostructure replicated from the stamp sheet.

6.1.4 Results

Figure 6.3 displays the AFM images of two types of nanostructures fabricated using thermal NIL.

For the first type of nanostructure, created using the pillar stamp shown in Figure 6.2(a), the AFM images in Figure 6.3(a), 6.3(b), and 6.4(a) showcase the results. The grating has a period of approximately $1\ \mu\text{m}$, with a nanostructure width of around $500\ \text{nm}$, a cavity width of around $500\ \text{nm}$, and a height of around $200\ \text{nm}$.

For the second type of nanostructure, produced using the grating stamp depicted in Figure 6.2(b), the AFM images in Figure 6.3(c), 6.3(d), and 6.4(b) demonstrate the results. The pillars have a period of approximately $500\ \text{nm}$, with a pitch diameter of around $400\ \text{nm}$, a cavity width of around $100\ \text{nm}$, and a height of around $150\ \text{nm}$.

Due to time limitations, only PMMA grating patterns were utilized for the subsequent experiments described in Section 6.2.

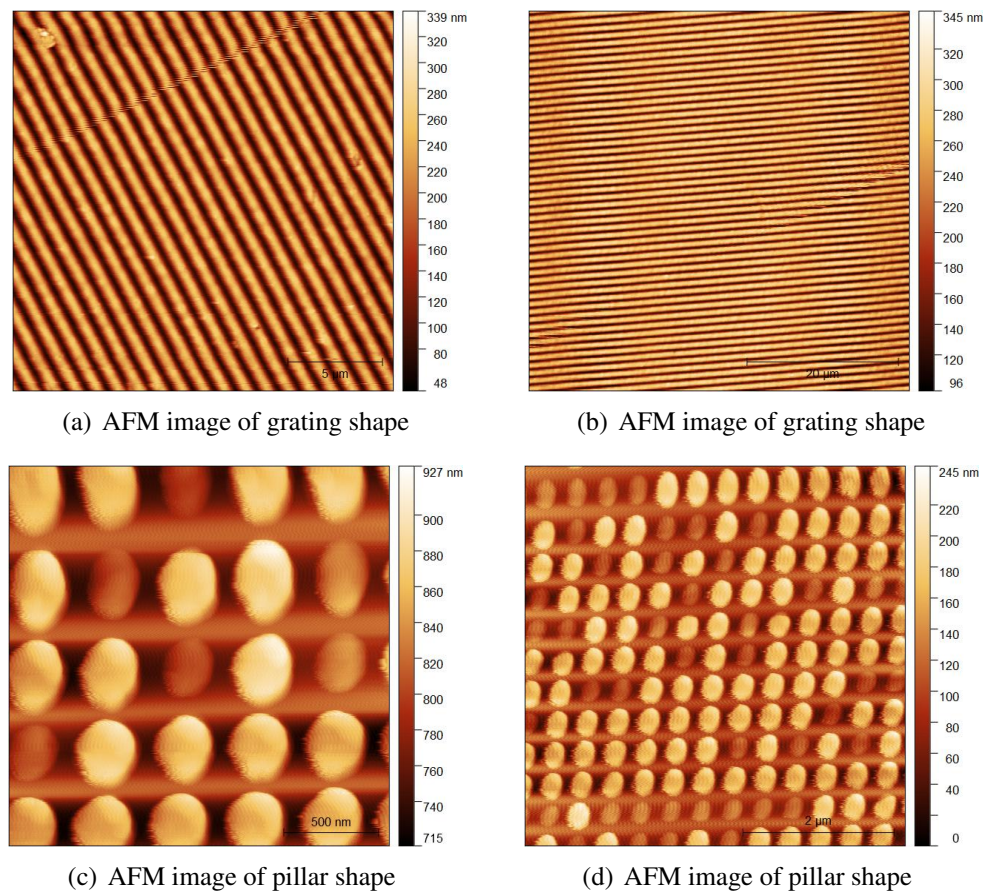
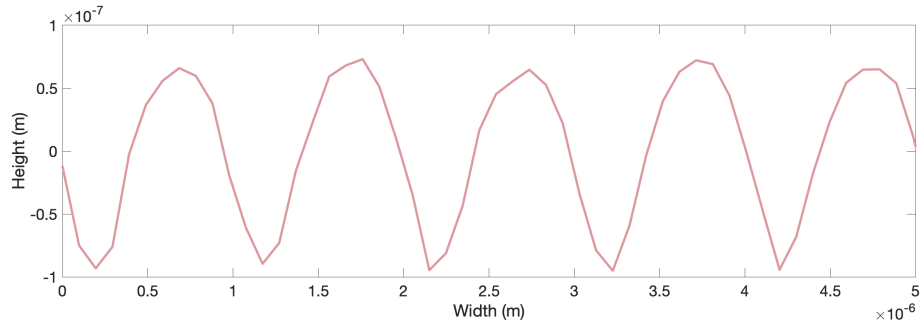
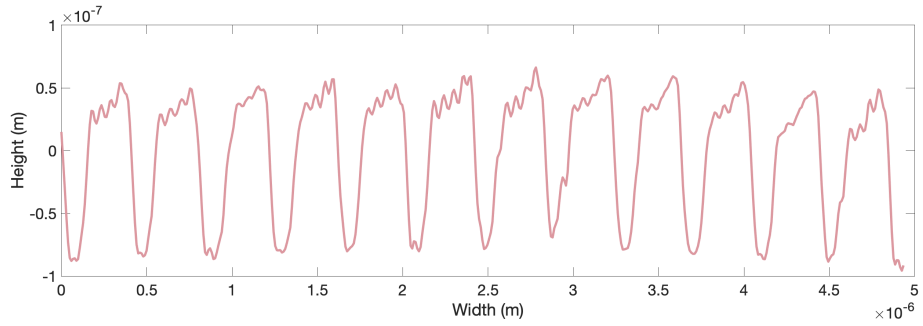


Figure 6.3: The AFM images of the nanopatterns



(a) grating sheets



(b) pillar sheets

Figure 6.4: The height vs width of nanopattern

6.2 OLED Fabrication

6.2.1 Introduction

Figure 6.5 shows the structure of OLEDs fabricated in the golve box.

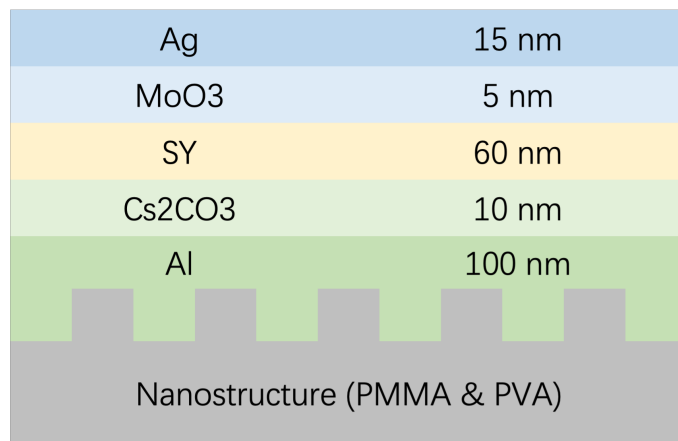


Figure 6.5: The structure of the fabricated OLED

6.2.2 OLED pixel architecture

Figure 6.6 depicts the design for the OLED pixel. The shadow mask used for the evaporation of Al (Aluminium) and Cs_2CO_3 (Cesium carbonate) is illustrated in Figure 6.6(a), where the red portion represents the deposition area. Figure 6.6(b) displays the shadow mask employed for the evaporation of MoO_3 (Molybdenum trioxide) and Ag (Silver), with the green region representing the deposition area. The yellow area shown in Figure 6.6(c) represents the pixel for the OLED, which emits light when a voltage is applied. The Pixel is defined as the overlapping area of the ITO and Aluminium Electrodes. For our devices a pixel area of 1mm by 2mm was chosen to enhance spectral signal to noise ratio.

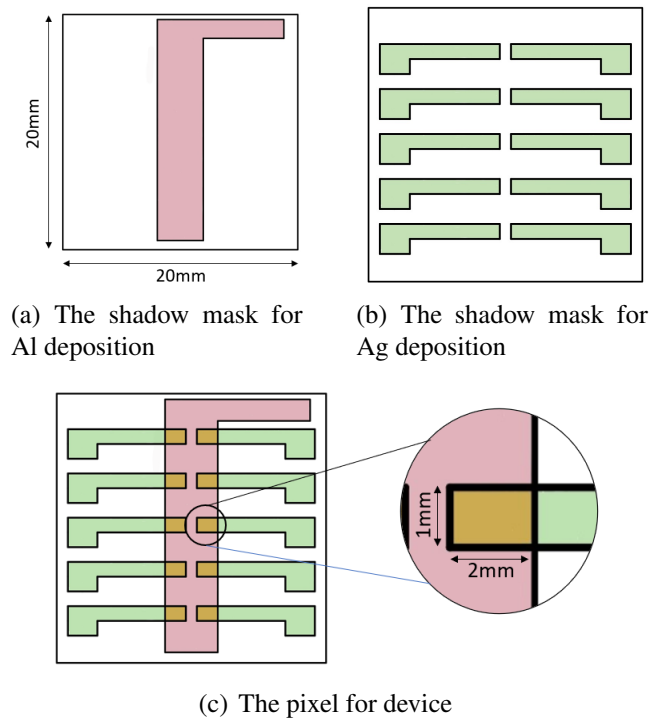


Figure 6.6: The shadow mask design

6.2.3 Material and Fabrication

The top-emitting OLED devices were fabricated using the following procedure. The glass substrates were first cleaned by subjecting them to ultrasonication in acetone and 2-propanol for 15 minutes each. A PMMA solution, prepared as described in Subsection

6.1.2, was then spin-coated onto the glass substrates. The nanostructure on the glass substrates was created using thermal NIL, as explained in Section 6.1.

Next, an aluminum (Al) layer with a thickness of 100 nm was deposited onto the glass substrates at a rate of approximately 0.5 A/second. This was followed by the deposition of Cs_2CO_3 with a thickness of 10 nm at a rate of around 0.12 A/second. These deposition processes were carried out inside an evaporation glove box (MBraun nitrogen glove box) with low levels of oxygen ($\text{O}_2 < 0.5$ ppm) and water vapor ($\text{H}_2\text{O} < 0.7$ ppm).

The emissive layer of the OLED device was prepared using Super Yellow (PDY-132, Sigma Aldrich) dissolved in toluene at a concentration of 7 mg/ml. A 60-nm-thick Super Yellow layer was achieved by spinning the solution at 3000 rpm for 60 seconds, followed by a 100 °C annealing step in a glove box (MBraun nitrogen glove box) with low levels of oxygen ($\text{O}_2 < 0.1$ ppm) and water vapor ($\text{H}_2\text{O} < 0.1$ ppm) for 20 minutes.

After annealing, the samples were transferred back to the evaporation glove box. Molybdenum trioxide (MoO_3) and silver (Ag) were sequentially deposited on top of the Super Yellow layer. The MoO_3 layer had a thickness of 10 nm and was deposited at a rate of 0.14 A/second, while the Ag layer had a thickness of 15 nm and was deposited at a rate of 0.2 A/second.

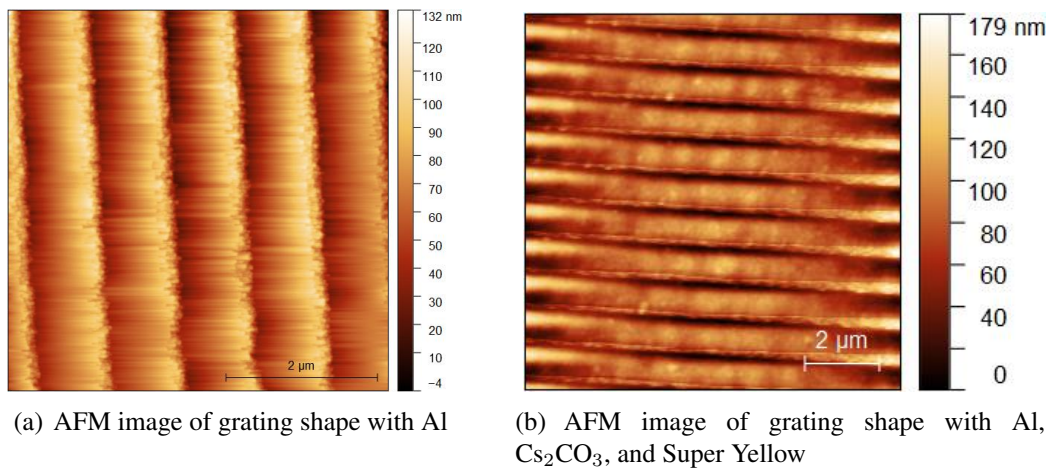


Figure 6.7: The AFM images of nanograting on OLEDs

Figure 6.8 presents the height measurements of the nanograting structure with different materials. Specifically, Figure 6.8(a) displays the size of the grating shape after the deposition of aluminum (Al), while Figure 6.8(b) illustrates the height of the grating shape after the deposition of Al and Cs_2CO_3 , as well as the spin coating of SY.

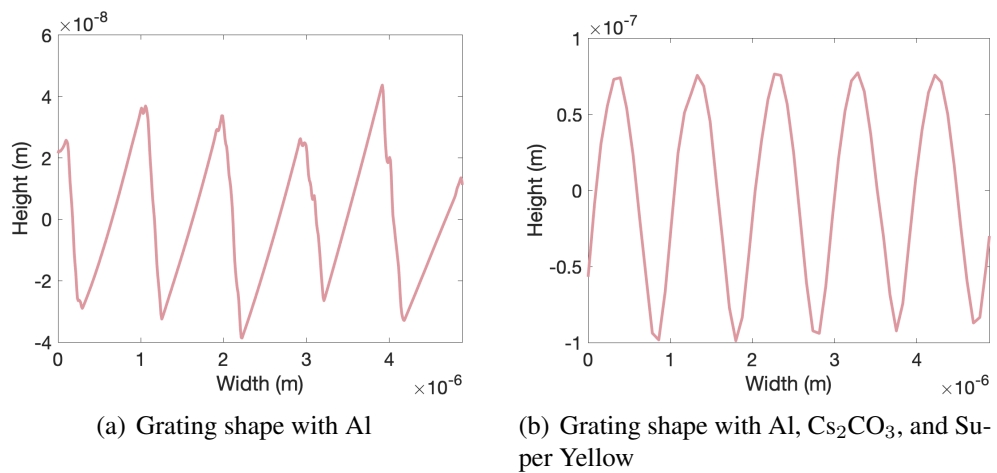


Figure 6.8: The height vs width

6.2.4 Results

Figure 6.9 illustrates the reflection characteristics of both flat and grating OLEDs. It can be observed that the reflection from the glass with the nanograting appears brighter compared to the flat OLED. This difference in reflection is attributed to the altered light path caused by the presence of the grating structure on the surface of the glass. In Figure 6.10,

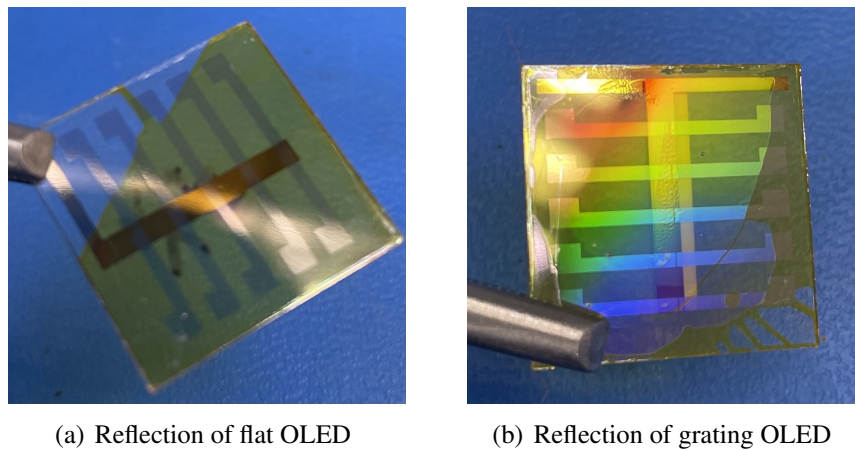


Figure 6.9: The reflection by eyes for flat and grating OLEDs

photos of both devices are displayed when a voltage of 10 V is applied. It is evident that the grating OLED emits a brighter light compared to the flat OLED. This enhancement in brightness can be attributed to the improved light outcoupling efficiency facilitated by the presence of the nanograting structure.

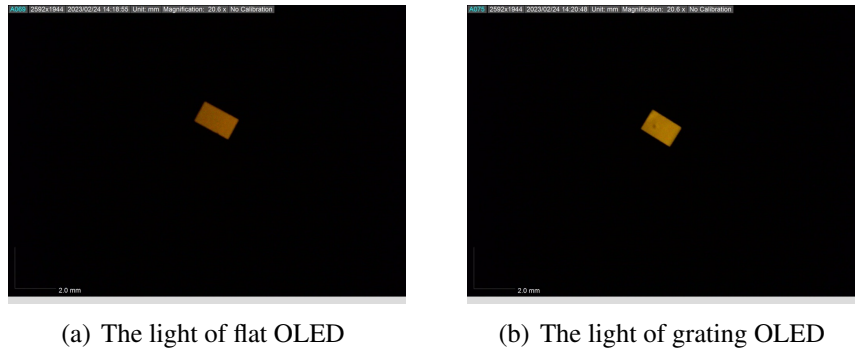


Figure 6.10: The light for flat and grating OLEDs with 10 V

Current-Voltage and Photocurrent Characteristics

Figure 6.11(a) depicts the current-voltage characteristics and the corresponding photon current as the input voltage is swept from 0 to 10 V. The current density, represented on the left-hand axis, remains relatively constant throughout the voltage sweep. However, the electroluminescence (EL) of the device, shown on the right-hand axis, exhibits a significant increase from approximately 3.5×10^{-7} to 6.4×10^{-7} as the voltage is increased. This corresponds to an increase of approximately 82.86% in EL intensity.

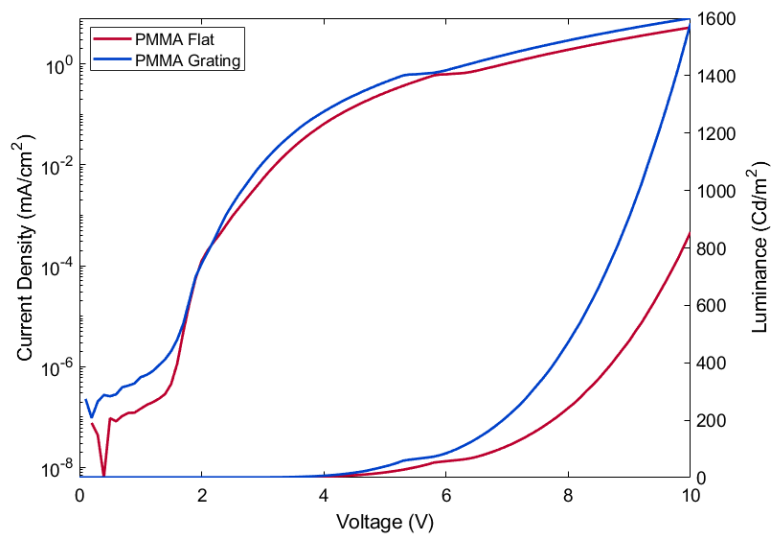
Figure 6.11(b) provides a logarithmic scale representation of the EL intensity. It can be observed that the turn-on voltage of the grating device is slightly lower than that of the flat device. This optimization in the turn-on voltage is achieved through the integration of the nanograting structure, further enhancing the performance of the device.

Spectral Response

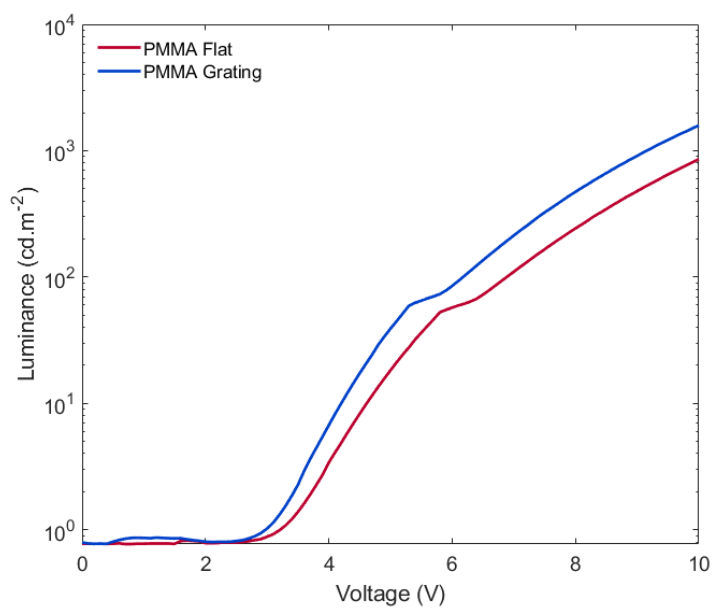
Figure 6.12 illustrates the emission spectra of the OLEDs with and without the nanograting structure. It can be observed that the integration of the nanograting has led to a slight narrowing of the emission spectrum. This narrowing indicates that the nanograting structure has influenced the emission properties of the device, potentially resulting in improved color purity or spectral selectivity.

EQE

While the absolute value of the luminance increased in the nanostructure device compared to the flat one, the enhancement in EQE was not as significant. It is important



(a) Current density and EL vs voltage for OLED



(b) EL vs voltage for OLED (log scale)

Figure 6.11: (a) Current density and EL vs voltage for OLED (b) EL vs voltage for OLED (log scale)

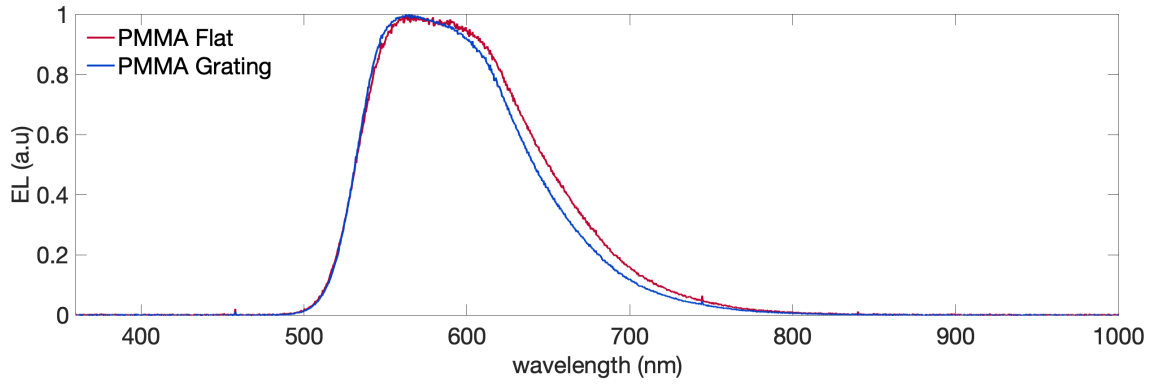
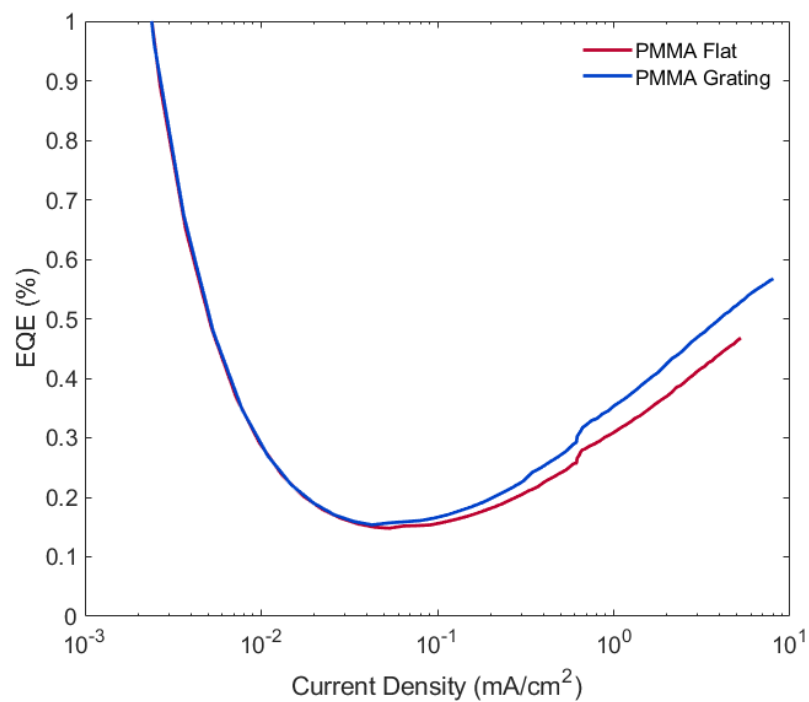
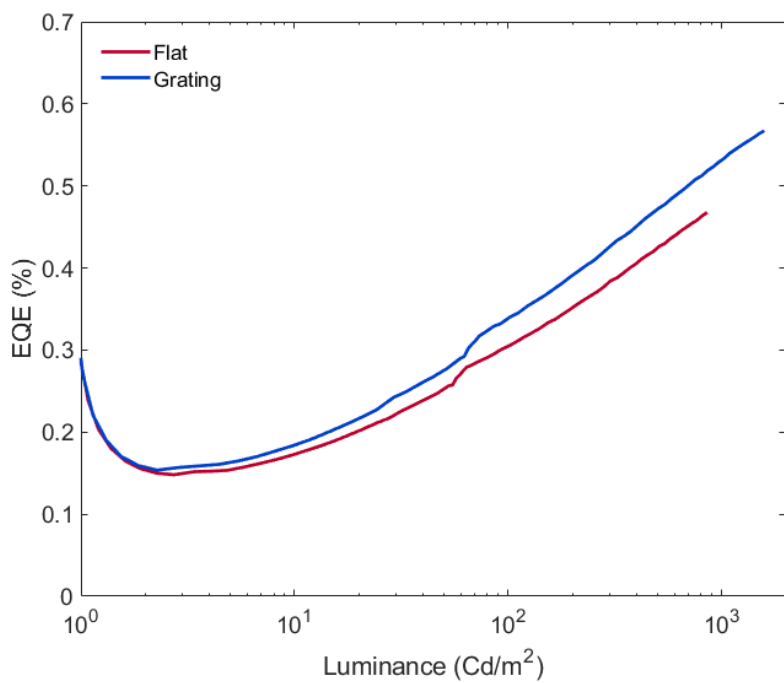


Figure 6.12: Spectrum of fabricated OLEDs

to consider the electrical characteristics when incorporating nanostructures into devices. The presence of nanostructures can introduce changes in the electrical behavior of the device, which may impact its overall performance and efficiency. Therefore, a comprehensive analysis of the electrical properties is necessary to fully understand the effects of nanostructures on device performance.



(a) EQE vs current density



(b) EQE vs luminance

Figure 6.13: a) EQE vs Current density for Flat and Grating OLED architectures, b) EQE vs Luminance for Flat and Grating OLED architectures

Reference

- [1] R. J. Fong, A. Robertson, P. E. Mallon, and R. L. Thompson, “The impact of plasticizer and degree of hydrolysis on free volume of poly (vinyl alcohol) films,” *Polymers*, vol. 10, no. 9, p. 1036, 2018. 6.1.3

Conclusion and Outlook

7.1 Conclusions

This report provides a comprehensive overview of the progress made in the Master's research project over a period of 12 months. The project focused on two main aspects: simulation and solution-processable organic light-emitting diodes fabrications.

The simulation results obtained using COMSOL Multiphysics demonstrated that the incorporation of appropriate nanostructures can significantly enhance the outcoupling efficiency (η_{out}) of the devices. The simulations allowed for the exploration of various parameters, such as the thickness of different layers and the size of nanostructures, to optimize the η_{out} . While OghmaNano is more focused on investigating the device's performance with the actual structure.

In addition to the simulations, experimental work was conducted to fabricate nanostructures using thermal nanoimprint lithography (NIL). The successful fabrication of nanostructures was confirmed, and these nanostructures were integrated with OLEDs. The experimental results showed that the integration of nanostructures effectively improved the overall device performance.

Overall, this research project successfully combined simulation and experimental ap-

proaches to enhance the performance of solution-processable OSCs devices. The findings and insights gained from this project provide valuable contributions to the field of organic electronics and pave the way for further advancements in the development of efficient and high-performance devices.

7.2 Future Work

The potential future work of this project will mainly focus on experimental investigations, particularly on integrating different nanopatterns onto optoelectronic devices such as OLEDs and LEFETs. Since the charge injection direction within OLEDs differs from that of LEFETs, further studies are necessary to understand the impact of nanostructures on charge injection within LEFETs.

Moreover, exploring the effects of material changes or adjustments in the thickness of each layer is crucial. By varying these parameters, it is possible to identify the potential advantages and challenges associated with different material combinations. This optimization process will help achieve the best fabrication parameters for enhancing the performance of the devices.

Additionally, the characterization and analysis of the device performance with specific emission layers should be pursued. By investigating the influence of different emission layer materials, their thicknesses, and other relevant parameters, it is possible to optimize the device's performance and improve its efficiency.

Overall, the future work will involve further experimental investigations to understand the impact of nanostructures on charge injection within LEFETs and to optimize the device performance through material selection and parameter optimization. These efforts will contribute to advancing the field of optoelectronic devices and unlocking their full potential in various applications.